

One-step Structure Prediction and Screening for Protein-Ligand Complexes using Multi-Task Geometric Deep Learning

Kelei He^{1,2†}, Tiejun Dong^{2,3†}, Jinhui Wu^{1,3*} and Junfeng Zhang^{1,2,3*}

¹State Key Laboratory of Pharmaceutical Biotechnology, Medical School of Nanjing University, Nanjing, P. R. China.

²National Institute of Healthcare Data Science, Nanjing University, Nanjing, P. R. China.

³School of Life Sciences, Nanjing University, Nanjing, P. R. China.

*Corresponding author(s). E-mail(s): jfzhang@nju.edu.cn; wuj@nju.edu.cn;

Contributing authors: hkl@nju.edu.cn; tiejundong@smail.nju.edu.cn;

†These authors contributed equally to this work.

Abstract

Understanding the structure of the protein-ligand complex is crucial to drug development. Existing virtual structure measurement and screening methods are dominated by docking and its derived methods combined with deep learning. However, the sampling and scoring methodology have largely restricted the accuracy and efficiency. Here, we show that these two fundamental tasks can be accurately tackled with a single model, namely LigPose, based on multi-task geometric deep learning. By representing the ligand and the protein pair as a graph, LigPose directly optimizes the three-dimensional structure of the complex, with the learning of binding strength and atomic interactions as auxiliary tasks, enabling its one-step prediction ability without docking tools. Extensive experiments show LigPose achieved state-of-the-art performance on major tasks in drug research. Its considerable improvements indicate a promising paradigm of AI-based pipeline for drug development.

1 Introduction

Small organic molecule (SOM) plays an important role in clinical treatment, accounting for about 72% FDA-approved drugs in 2018 ~ 2022[1]. Its efficacy is achieved by binding to the target (usually a protein) as a ligand, to produce a protein-ligand complex. Understanding the structural details of the protein-ligand complexes at the atomic level reveals the bioactivities of the proteins and ligands, thus guiding the structure-based drug development, *e.g.*, drug screening[2, 3, 4] and lead optimization[4, 3, 5]. Conventional methods use experimental measurements (*e.g.*, X-ray diffraction[6] and cryo-electron microscopy[7]) to analyze novel protein-ligand complexes, however, are time and resource-expensive.

To alleviate this problem, virtual measurement by molecular docking[8, 2, 9, 4] has been widely adopted in the past decades to predict the native-like ligand-binding conformations with the respective protein-binding sites. Typically, a docking tool first samples a set of binding conformations (namely poses), and then ranks them using a scoring function to select a top-scored pose[9] (Fig. 1b). As reported, popular docking tools generate native-like poses with accuracies from approximately 40% to 60% in terms of success rate[10], which were far from satisfactory. Since deep learning has impacted the field of drug development, many researchers attempted to build hybrid methods by regarding it as a more expressive scoring function to rank the poses sampled by conventional docking tools[11, 12, 13, 14, 15, 16]. Nevertheless, the performance of these hybrid methods has a constrained upper bound, as limited by the sampling time and space of docking tools[15].

Recently, several deep learning methods, *i.e.*, AlphaFold[17], RoseTTAFold[18], and ESMFold[19], have shown great capacity to predict protein structures that outperformed previous methods by a large margin. These methods provided a novel computational approach to generate protein structures directly from their chemical sequences, rethinking the structure prediction paradigm in a data-driven perspective without following the conventional force-field assumption[20]. Recent progresses[21, 22, 23, 24] demonstrated that using these methods as the protein/peptide structure estimator can predict precise structures for amino acid-based complexes such as the protein-protein and protein-peptide complexes, showing the generalizability of deep learning methods to the downstream tasks. However, these methods are not specifically designed for SOM ligands, which inevitably restricts the related applications such as protein-ligand complex structure prediction and virtual screening. As these two fundamental tasks have heavily relied on docking tools in the past four decades[25, 26, 27, 28], developing a deep learning model that provides refined atomic complex structure and screening for the protein-ligand pairs is highly demanded.

To this end, we introduce LigPose, a novel docking-free geometric deep learning method to accurately predict the native-like conformation of ligands with their corresponding protein targets and the respective binding strengths in one step (Fig. 1c). Specifically, for a given protein and ligand pair, the

ligand and its binding target are jointly represented as a complete undirected graph, with each node denoting an atom, and all nodes are mutually connected. Then, their 3-D structures are directly optimized by the atom coordinates in the Euclidean space, with the binding strength and the correlation-enhanced graph learning jointly learned as auxiliary tasks (Fig. 1d).

Based on the ability to represent the inter-atom relationships, LigPose achieved state-of-the-art performance on major tasks in drug development, *i.e.*, structure prediction, virtual screening, and affinity estimation. Notably, LigPose outperformed 12 existing docking tools with a significant improvement of 14% in terms of success rate on conformation prediction, with an up to 1851x faster inference speed. Moreover, our method performs even better on the more challenging and practical tasks, *i.e.*, cross-docking and virtual screening, with greatly higher improvements of 20.1% and 19.3% in terms of success rate, respectively, compared with the existing best-performing method. Evaluations on SARS-CoV-2 M^{Pro} complex structure prediction show LigPose obtained 18.2% improvements compared with docking tools, revealing its robustness in real environments. Despite the high accuracy and speed, the qualitative analysis showed that LigPose has the interpretability to learn non-covalent interactions even without explicitly incorporating the physical or chemical priors, *e.g.*, the energies, which are usually regarded as the core idea of building structure prediction methods. The superior performance of LigPose suggests a promising paradigm for structure-based drug design using deep learning. We hope this work can facilitate the research of drug development.

2 Results

2.1 LigPose pipeline

LigPose predicts the 3-D structure of the ligand-binding conformation with its protein target in an end-to-end manner. As shown in Fig. 1c, a given protein and ligand are jointly represented by a complete undirected graph, where each atom is denoted as a node, representing its chemical feature and coordinate, and all nodes are mutually connected. Since the entire protein-ligand graph is large, LigPose (Fig. 1d) first adopts a sampling and recycling strategy, to predict with multiple cycles, where each cycle updates a randomly sampled sub-graph. The features and coordinates within the sub-graph are then processed by the proposed feature and coordinate update blocks. These two blocks are built on the graph neural network and stacked 6 times with unshared weights. The key design of these two blocks is to leverage the inter-atom distances during network forwarding for maintaining the spatial information, making the predicted atom coordinates insensitive to their initial positions, but influenced by the inter-atom correlations. Finally, a symmetric-aware loss is proposed to optimize the network, combined with a stochastic coordinate initialization strategy for the ligands, to enable the method of distinguishing the ligand atoms with the same chemical features. The affinity and screening

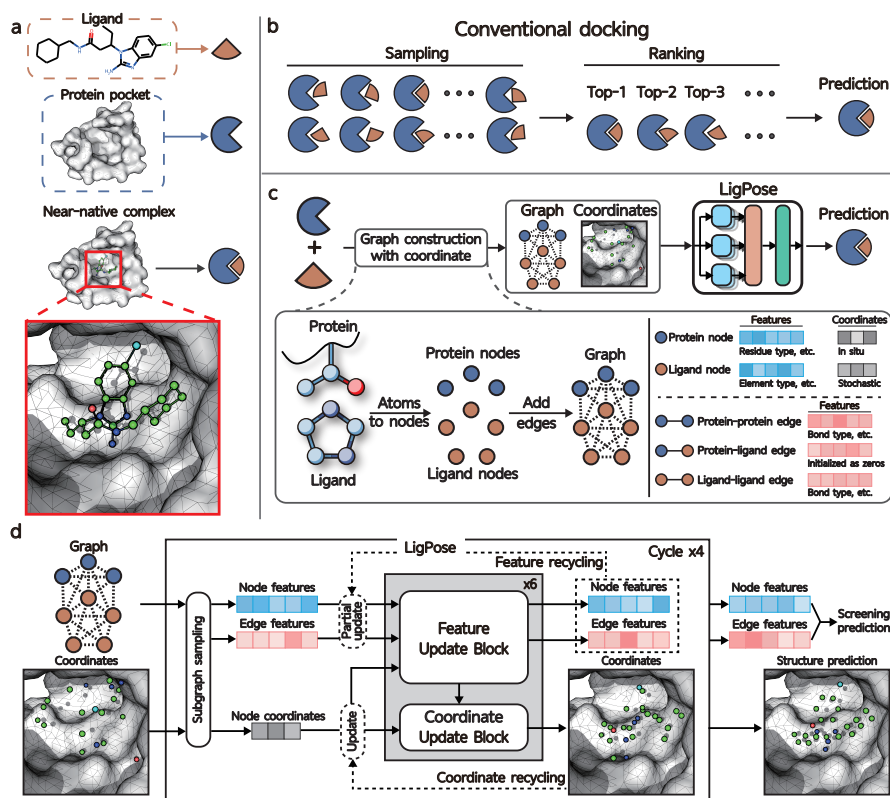


Fig. 1 LigPose predicts ligand-protein complex structure using geometric deep learning in an end-to-end manner, compared with the conventional docking method. (a) Notations of a ligand, a protein pocket, and their complex. (b) The pipeline of the conventional docking tool consists of two stages, *i.e.*, sampling and ranking[9]. (c) The pipeline of our method. (d) Architecture of LigPose.

efficacy are learned by two additional prediction heads as auxiliary tasks. Moreover, we adopt self-supervised learning of the atomic correlations on large-scale unlabeled data including millions of random protein-ligand pairs without characteristics, to improve the generalizability of LigPose to unknown molecules. An ablation study of LigPose is illustrated in Suppl. Sec. A.9.3. Please refer to Methods, Suppl. Methods and Fig. A3 for more details of the method.

2.2 Predicting accurate complex structures

In experiments, we first focus on the flexible-ligand prediction with the determined protein pockets, a widely used setting in structure-based drug development[30], to demonstrate its effectiveness. We compare LigPose with 12 popular docking tools on the refined set of PDBbind database[31, 10]. The PDBbind database collects a large set ($N = 19443$) of 3-D biomolecular complex structures from the PDB database. The refined set ($N = 5316$) and the

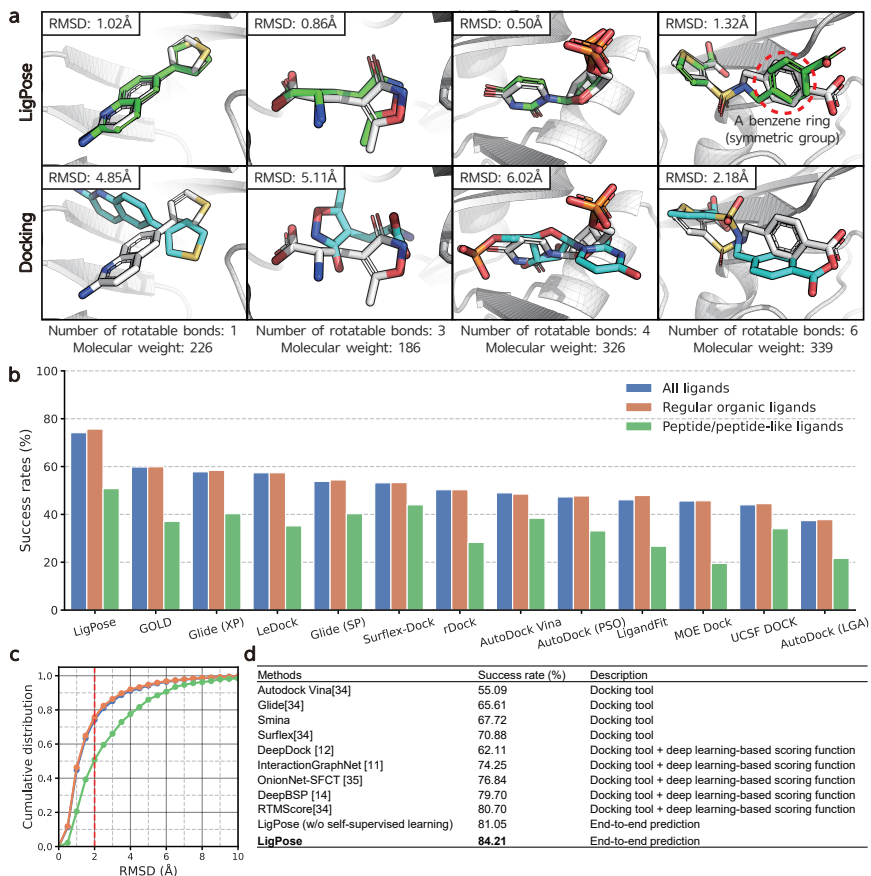


Fig. 2 Performance of LigPose on ligand-binding conformation prediction compared with popular molecular docking tools and hybrid deep learning methods. (a) Visualization of the generated poses of LigPose and a docking tool (Smina[29]) for four ligands with various weights and number of rotatable bonds (PDB codes: 3RSX, 1P1Q, 3DXG, 4JXS). The native poses, predictions of LigPose, and docking tools are denoted as white, green, and cyan backbones, respectively. Within the predictions, the oxygen and nitrogen atoms are denoted as red and blue colors, respectively. (b) Quantitative comparison of success rate between LigPose and the top-scored poses generated by 12 docking tools on the refined set of PDBbind. (c) Cumulative distribution of RMSD of LigPose. The red dashed line indicates the RMSD threshold of 2Å. Blue, orange, and green colors denote all ligands, the regular organic ligands, and the peptide/peptide-like ligands, respectively. (d) Quantitative comparison of success rate between LigPose, the docking tools, and the hybrid deep learning methods on the core set of PDBbind.

core set ($N = 285$) are derived from PDBbind with high data quality regarding the crystal structures, binding data, and the nature of complexes[32].

The visualization of the predicted poses in Fig. 2a shows LigPose is able to predict accurate poses for ligands of various flexibilities on those that are failed by docking tools. It is worth noting that the symmetric structures (*i.e.*, atoms

in a benzene ring) are predicted in the right place. The quantitative comparison of the success rate between LigPose and 12 popular docking tools with top-scored poses is shown in Fig. 2b. The predicted poses with Root Mean Square Deviation (RMSD) less than 2Å to their native poses are regarded as successful predictions[10]. As suggested by the figure, LigPose obtains a high success rate of 74.1% on the entire refined set. Compared with a previous study that reported on a subset ($N = 2002$) of the refined set[10], LigPose achieves 73.3%, which is 13.5% higher than the best record docking tool (GOLD[33] with 59.8%). The other docking tools have unsatisfied success rates, ranging from 37.4% (AutoDock (LGA)[34]) to 57.8% (Glide (XP)[35]). In addition, we observe the peptide/peptide-like molecules with more rotatable bonds and weights are more challenging to predict than the regular organic ligands, leading to performance degradation for both LigPose and docking tools. Considering the predicted poses with $\text{RMSD} < 4\text{\AA}$ (Fig. 2c), LigPose achieves the success rate of above 90% on regular organic molecules, shown effectiveness on near-native structure prediction for conformations.

We also report the performance of LigPose on regular organic molecules compared with the docking tools with the best poses in Suppl. Fig. A6. Herein, the best pose denotes the pose of the lowest RMSD among all sampled poses and reveals the performance upper bound of the docking tools. The figure shows the success rate of LigPose (74.6% and 58.4%) outperforms 8 and 10 docking tools for regular organic and peptide/peptide-like ligands, respectively. These results indicate that the majority of those docking tools could not have a chance to outperform LigPose by improving the scoring functions[15], since they cannot produce correct pose candidates in limited sampling steps for some ligands that are correctly predicted by LigPose.

To conduct a fair comparison with the deep learning-based methods, we performed LigPose on the core set, a well-designed but smaller subset of PDBbind. Here we summarized the success rates of LigPose with diversified methods, including docking tools and state-of-the-art deep learning-based methods[14, 11, 12, 36, 37] in Fig. 2d, where LigPose obtained the success rate of 84.2%, which is higher than the best-performing method RTMScore (80.7%), indicating the high performance of the proposed end-to-end paradigm. Besides, we extend LigPose to work as a scoring function (see Suppl. Results Sec. A.9.1 and Fig. A1) to make it compatible with the existing docking tools, which also achieves comparable results to the state-of-the-art scoring functions.

We further test LigPose on cross-docking, a more challenging and practical task in drug screening[38, 39]. Cross-docking aims to produce the binding conformation for a ligand, from which the target protein is experimentally determined by a complex with another ligand[38]. The experiments are implemented on the PDBbind-CrossDocked-Core set ($N = 1343$ pairs, derived from the core set[39]), where LigPose achieves the highest success rate of 72.0%, with a greatly large improvement (20.1%) compared to the second-best method (*i.e.*, RTMScore, 51.9%), as shown in Suppl. Table A8, revealing a more generalizable method of LigPose compared with existing competitors. Moreover, the

success rate of LigPose shows improvements of 5.3% to 20.1%, compared with three docking tools using the best-sampled poses (51.9% to 66.7%), suggesting the advances of the data-driven approach.

2.3 Ligands with various flexibilities

To solve the ligands with high flexibilities (*i.e.*, with many rotatable bonds), the strategies of sub-graph sampling and recycling are combined to progressively refine the predictions. We visualize the ligand atoms and plot the RMSD trajectories for two representative samples in Fig. 3a, where one is heavier with more rotatable bonds (PDB code: 1EBY) than the other (PDB code: 1O5B). As a hard example, the prediction of 1EBY reaches the threshold of 2Å after 16 updates, which is much slower than that of 5O87 (with 5 updates), indicating the effectiveness of the proposed recycling strategy.

To quantify the performance of LigPose concerning the number of rotatable bonds, we plot the results of LigPose and Smina on the refined set in terms of RMSD (b) and success rate (c) in Fig. 3. One can observe is the difficulty of prediction is positively correlated with the number of rotatable bonds. We suppose the reason is that more rotatable bonds indicate higher flexibility of the ligand. Although the success rates of LigPose and Smina are both decreased when predicting ligands with many rotatable bonds, LigPose performed consistently better than Smina through the dataset. Moreover, Smina failed to predict with more than 24 rotatable bonds, indicating the limited processing power of the docking methods. By contrast, LigPose correctly predicted 20% of them, showing the merit of our learning-based methodology. Similar findings were discovered from the core set, as shown in Suppl. Fig. A7.

The efficiency is also a core factor of drug development[40], caused by a large number of drug-like molecules for screening and measurement. We then plot the inference time per ligand with respect to the number of ligand rotatable bonds for LigPose and Smina in Fig. 3d. For a fair comparison, we use a single CPU core to implement docking tools and LigPose (CPU), with only an additional common GPU device (Nvidia GTX 2080Ti) for the GPU version (LigPose (GPU)). From the figure, we observed the inference time of LigPose is constant, in contrast to that of docking tools, which is positively correlated with the number of rotatable bonds. On average, LigPose inferences 4 – 26 (CPU) / 303 – 1851 (GPU) times faster than docking tools. For ligands with more than 10 rotatable bonds, LigPose can infer 7299x times faster than docking tools, and up to 14256x faster for ligands with more than 20 rotatable bonds.

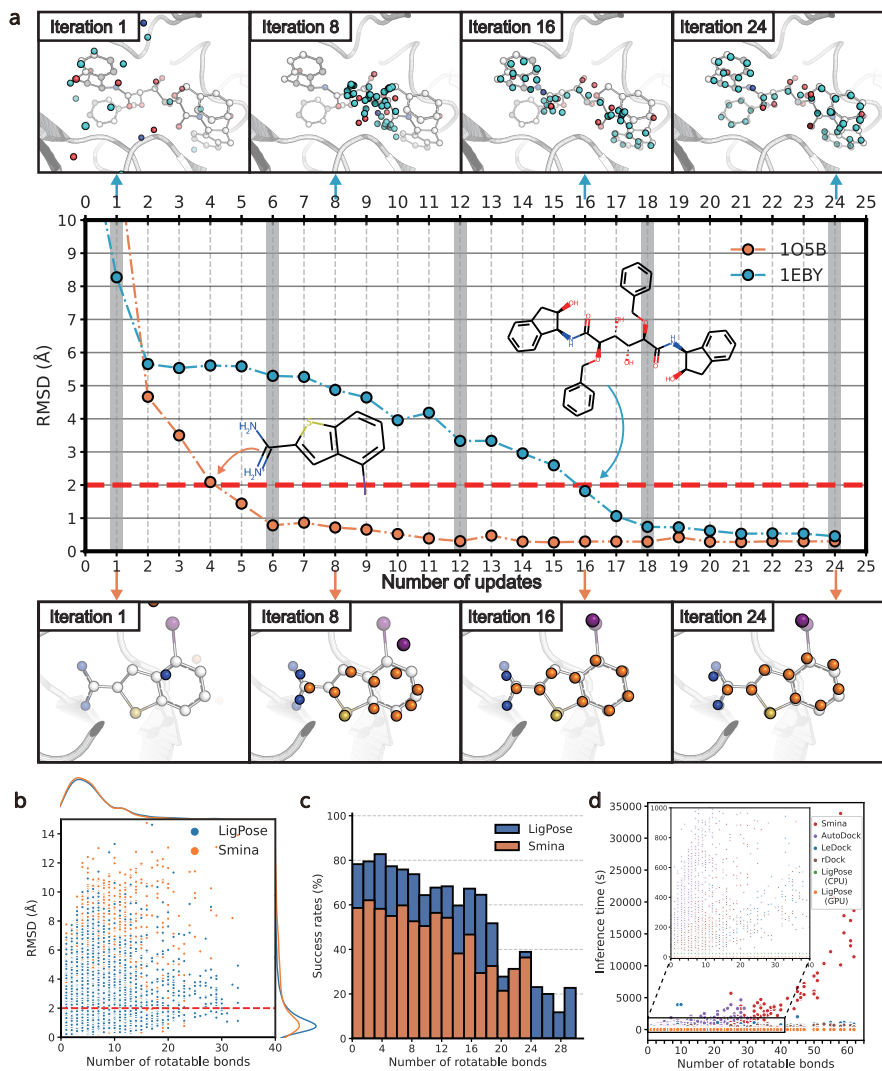


Fig. 3 Performance of LigPose with respect to the ligand flexibility. (a) RMSD trajectory of two representative samples (PDB codes: 1O5B and 1EBY). LigPose updates a given ligand 24 times using 4 cycles, with each cycle updating the ligand 6 times. The ligand atoms in the {1, 8, 16, 24}th updates are visualized at the panel's top and bottom. The predicted atoms are denoted with orange and cyan colors for 1O5B and 1EBY, respectively. The oxygen, nitrogen, and iodine atoms are denoted with red, blue, and purple colors, respectively. The native poses are placed in the background with a grey color. (b–c) RMSD (b) and success rate (c) for ligands with respect to the number of rotatable bonds on the core set of PDBbind. The red dashed line indicates the RMSD threshold of 2Å. (d) Inference time of LigPose and four popular docking tools on 1000 randomly selected samples in the PDBbind dataset.

2.4 Accurate and fast screening

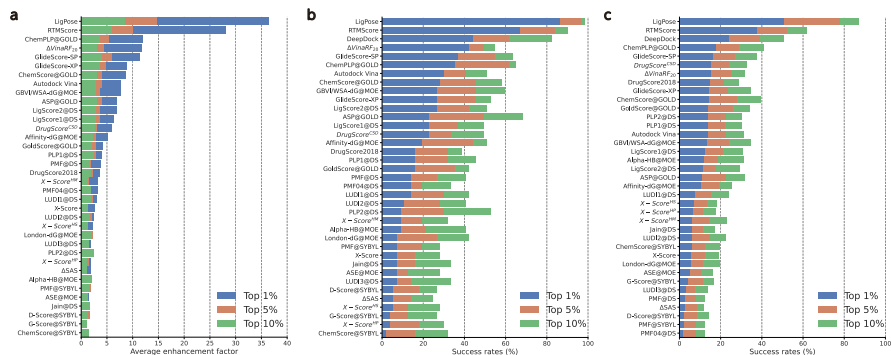


Fig. 4 Screening power of LigPose on the CASF-2016 benchmark. (a) Average enhancement factors of forward screening. (b) Success rates of forward screening. (c) Success rates of reverse screening.

Accurate prediction of the complex structure is an essential procedure, and ideally beneficial for the virtual screening task. Therefore, we validate the screening power of LigPose using the CASF-2016 benchmark, which contains 57 proteins, each having at least 5 true binders with a wide range of affinities. Therefore, for each SOM-protein pocket pair, LigPose predicts the potential binding strength of SOMs to the protein pockets as the screening score, through the multiplication of the predicted binding probability and affinity.

As suggested by Fig. 4, LigPose outperformed the state-of-the-art methods in all three metrics with a very large performance gap, compared with recent deep learning-based methods and popular conventional methods. Concretely, for the forward screening, *i.e.*, the task of identifying true binding SOMs for a certain protein, LigPose gets an average enhancement factor (EF) of 36.4%, and a success rate of 86.0% on top 1%-ranked SOMs. These results are greatly higher than that of the second best performing method RTMScore[36] (with EF of 28.0% and success rate of 66.7%), with improvements of 8.4% and 19.3% on EF and success rate, respectively. It also largely outperforms recent deep learning-based methods, *i.e.*, DeepDock[12] (with EF of 16.4% and success rate of 43.9%) and PIGNet[41] (with EF of 19.36% and success rate of 55.4%). Besides, the results show huge gaps to conventional methods (with EFs ranging from 0.8% to 11.9% and success rates ranging from 1.8% to 42.1%). For top-5% and top-10% ranked SOMs, similar conclusions can be made. Notably, LigPose reaches very high success rates of 96.5% and 98.2% on top-5% and top-10% ranked SOMs, suggesting that nearly all true SOM binders are settled at the top of the predictions. Similarly, for the reverse screening, *i.e.*, the task of identifying true binding proteins for a certain SOM, LigPose obtains success rates of 50.5%, 77.9%, and 87.0% in top-1%, top-5%, and top-10% ranked

proteins, respectively. It also outperforms RTMScore[36] (with 37.6%, 52.4%, 62.1%) and DeepDock[12] (with 23.9%, 39.3%, 50.9%) by a large margin.

The superior screening ability of LigPose benefits from its state-of-the-art performance on drug-target affinity estimation (see details described in Suppl. Results Sec. A.9.2 and Table A1). Notably, LigPose provides accurate affinity estimation without requiring native complex structures.

2.5 Validating on the SARS-CoV-2 M^{Pro}

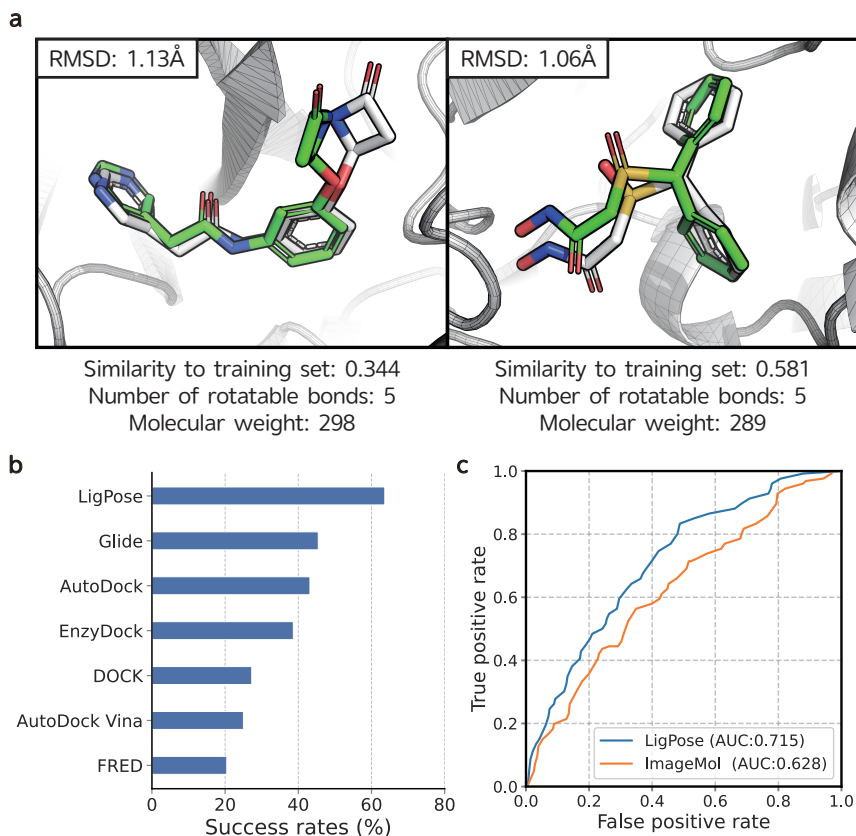


Fig. 5 Applications of LigPose on drug research for SARS-CoV-2 M^{Pro}. (a) Two visualized samples of M^{Pro} complexes (PDB codes: 5RGU and 7ANS). Predictions of LigPose are denoted as green and cyan backbones. Within the predictions, the oxygen, nitrogen, and sulfur atoms are denoted as red, blue, and yellow colors, respectively. (b) Success rates of structure prediction for M^{Pro} complexes. (c) Success rates of virtual screening for M^{Pro} inhibitors.

We further validate LigPose on the main protease (M^{Pro}) of severe acute respiratory syndrome coronavirus 2 (SARS-CoV-2) to demonstrate its efficacy in real-world applications. M^{Pro} plays a critical role in virus replication as a

hot-spot target for anti-SARS-CoV-2 therapy[42]. In this work, two tasks are considered, *i.e.*, structure prediction and inhibitor discovery.

The structure prediction ability is assessed on a recently developed benchmark, which provides a baseline of 6 commonly-used docking tools on 44 M^{Pro} complex structures[43]. We visualize two typical samples in Fig. ??a, where LigPose successfully predicts binding conformations of these novel inhibitors (Tanimoto similarities[44] of 0.344 and 0.581 to their most similar molecules in the training set using Morgan fingerprint[45]). For the quantitative comparison of all 44 complexes as shown in Fig. 5b, LigPose achieves a success rate of 63.64% with a significant improvement of 18.19%, compared with the best-performing docking tool (*i.e.*, Glide, 45.45%). The success rates of other docking tools are much lower in the range of 20.45% to 43.18%.

We validate LigPose on screening M^{Pro} inhibitors on a dataset ($N = 344$) derived from DrugCentral[46]. The results in Fig. 5c show LigPose obtains an Area Under Curve (AUC) of 71.5%, with an improvement of 8.7% compared with the recent deep learning-based methods ImageMol (62.8%)[47].

2.5.1 Learning non-covalent interactions

In addition to the effectiveness and efficiency, LigPose also showed good interpretability by investigating its ability to reconstruct the non-covalent interactions. We used a metric, namely interaction reproducibility, to quantify this ability, following the work in [48] (see Methods for details).

From Fig. 6a, we observed the interactions are well reconstructed by LigPose on predictions with $\text{RMSD} < 2\text{\AA}$, and have lower scores on predictions with $\text{RMSD} \geq 2\text{\AA}$. For each type of interaction (Fig. 6b), LigPose performed best for hydrogen bond and water bridge and showed insensitive to π -cation and halogen bond. We suppose the reason is the lack of respective ligand samples. We further compared the performance of LigPose with Smina (Suppl. Figs. A8 and A9), and found that LigPose showed consistently better performance for all the seven types of interactions.

In addition to the high quantitative scores, we further inspected the attention weights, by visualizing three representative complexes with respect to three non-covalent interactions (*i.e.*, hydrophobic interactions, salt bridge, and π -stack) in Fig. 6(c-f). We observed from the figure that LigPose can capture some potential interactions between ligands and proteins, without explicitly using related physical or chemical prior knowledge.

3 Discussion

In this work, we propose LigPose, which can predict protein-ligand complex structure, affinity, and screening probability simultaneously using multi-task geometric deep learning. The protein-ligand pair is first presented by one complete undirected graph, then, LigPose with a graph transformer network structure, directly predicting the complex structure in three-dimensional space. To precisely predict the complex structure with atomic accuracy, LigPose is

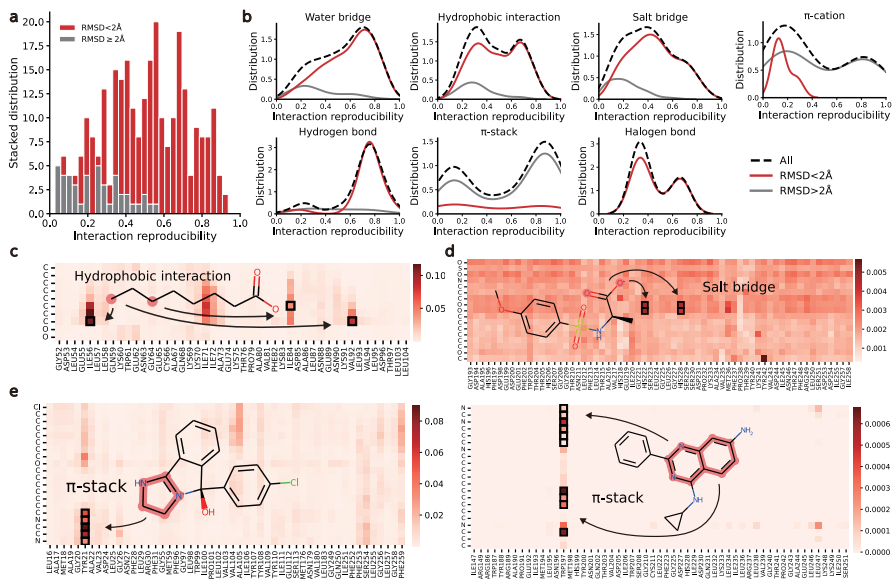


Fig. 6 LigPose implicitly learned non-covalent interaction patterns. **(a)** Stacked distribution of interaction reproducibility for all non-covalent interactions on the refined set. The red and grey colors denote $\text{RMSD} < 2\text{\AA}$ and $\text{RMSD} \geq 2\text{\AA}$, respectively. **(b)** Distribution of the interaction reproducibility for seven specific non-covalent interactions. Distribution of all samples, the samples of $\text{RMSD} < 2\text{\AA}$ and $\text{RMSD} \geq 2\text{\AA}$ are denoted in black, red, and grey dashed lines, respectively. **(c-f)** Visualization of attention weights in LigPose for three representative protein-ligand complexes. The attention weights with the red color from light to deep indicate the probability of non-covalent interaction between a ligand atom and a protein residue from low to high. Black boxes denote non-covalent interactions of native structures in the attention maps for hydrophobic interactions (PDB code: 3NQ9) **(c)**, Salt bridge (PDB code: 3EHY) **(d)**, and π -stack (PDB code: 4MME/4DLI) **(e,f)**. Attention weights are visualized at the atom level for ligands and residue level for proteins.

equipped with three innovations. To be specific, 1) we use a sampling and recycling strategy to optimally learn the protein information by multiple cycles, to handle a large number of protein nodes while reducing the computation burden. In each cycle, the feature update block is used to extract latent features for graph nodes and edges, and the coordinate update block updates the coordinates of all atoms (nodes) to their near-native 3-D position. Besides, 2) we design a specific atom initialization strategy and a symmetric-aware loss function for symmetric structures of the ligands. 3) We adopt a multi-task learning framework to train LigPose on all tasks, and leverage the power of self-supervised learning on large-scale unlabeled protein-ligand pairs, making the model more generalized to novel molecules. These advances obtained a notable improvement in the tasks of drug development.

LigPose correctly predicted 3914 (74%) ligand structures (with $\text{RMSD} < 2\text{\AA}$) on the refined set of PDBbind, which significantly outperformed 12 popular docking tools by 14%. LigPose also performed better than recent

hybrid deep learning methods on the core set. Many pieces of research in this field focused on building hybrid methods[13, 15, 14, 11, 49, 16]. However, as we demonstrated in experiments (Fig. 2e), these methods are limited by the sampling power of the docking tools[15]. Indeed, exhaustively exploring the sampling space dramatically increases the runtime, making it impractical in real-world drug screening. Recently, Oscar *et al.*[12] proposed DeepDock, which used geometric deep learning to build a docking-like method. Interestingly, this method could be regarded as a deep learning-based scoring function from a global perspective. However, this method in a docking-like fashion will also face the same challenges as docking tools in both effectiveness and efficiency. For instance, they reported that 60 out of 285 samples failed to find a minimum, and only 62% (177) out of 285 samples were successfully predicted on the core set, leading to unsatisfied performance even worse than conventional docking methods (Fig. 2e). By contrast, LigPose overcomes these limitations by directly optimizing the atom coordinates without sampling and energy-based minimizing, suggesting a novel computational paradigm for the prediction of the protein-ligand complex structures, coincident with AlphaFold in the task of protein structure prediction[17]. In a more challenging task, *i.e.*, cross-docking, LigPose shows tremendous success with an improvement of 20.1% in terms of success rate compared with the best-recording deep learning method RTMScore. Unlike the commonly used re-docking task adopted by previous methods (*e.g.*, DeepDock, DeepBSP), cross-docking is more practical in real-world situations.

In addition to the high performance, LigPose also infers considerably faster than docking. In real-world drug development, methods are expected to accurately screen a tremendous number (*i.e.*, up to 10^{60} [50]) of drug-like molecule candidates[2, 51]. Unfortunately, the docking-based methods with an iterative sampling strategy have suffered from the efficiency problem for a long time. Many studies tried to solve the problem by implementing CPU/GPU parallel acceleration algorithms in favor of engineering[52, 53, 54]. Besides, some works combined deep learning with conventional docking tools to boost the inference speed[55, 56]. We suggest that LigPose with an efficient end-to-end learning framework could be an alternative choice for docking to accelerate drug development.

Precise structure prediction naturally promotes drug screening, which is dominated by docking in large-scale structure-based drug development. Thus, structure-based deep learning methods[55, 57, 36] also prefer incorporating the compute-intensive docking tools, which limit their accuracy and efficiency. Other than the structure-based methods, several recently developed deep learning methods, including image-based (*i.e.*, using molecule image)[47], graph-based (*i.e.*, using molecular graph)[58, 59, 60, 61], and sequence-based (*i.e.*, using Simplified molecular input line entry system (SMILES))[62, 63, 64], learn informative representations of SOMs, showing promising performance in the binary classification of binding candidates. However, these ligand-based methods lack consideration for protein structure (or sequence), resulting in

providing a black box method without actual atomic interactions between proteins and ligands. LigPose provides a more reasonable solution to combine the structure basis and protein-ligand interactions for drug screening. Therefore, LigPose achieves the state-of-the-art affinity estimation and virtual screening performance without leveraging the native complex structures, showing its feasibility to real applications. Our further validations on SARS-CoV-2 M^{Pro} structure prediction and inhibitor screening indicate that LigPose meets the requirements for real drug development.

Building an accurate automatic drug development pipeline has encouraged decades of exploration[65, 20]. Recent advances demonstrated that protein structures can be accurately predicted by AlphaFold[17] and RoseTTAFold[18]. Therefore, predicting the structure of biomolecular complexes could be naturally considered as a subsequent application, as also suggested by Baek *et al.*[20]. In addition, the task of identifying the protein pocket has been well-addressed by existing works[66, 67, 68, 69]. Inspired by these successes, integrating LigPose with the aforementioned methods is appropriate, carrying out a promising end-to-end pipeline of drug screening directly from the protein sequence and the ligand chemical formula.

Moreover, in the field of structural biology, recent attempts have extended the application scenario of artificial intelligence to design the protein structures[70, 71]. A similar idea could also be applied to drug development. However, existing methods proposed to design (or generate) novel drug candidates neglected to consider either the 3-D structures or the protein-drug interactions[72, 73, 74, 61, 75, 76, 77, 78, 79]. Here, we suggest that LigPose has the potential to build novel end-to-end drug-generation methods with both refined structural details and confident bioactivity prediction, to boost de novo drug design, which can be regarded as future work.

4 Methods

4.1 Data collection

4.1.1 Benchmark Dataset

Training and validation dataset. We use the *general set* of PDBbind database (version 2020)[31] to develop and validate LigPose, consisting native structures of 19443 protein-ligand complexes. Within the general set, two subsets are used for evaluation, *i.e.*, the *refined set* and the *core set*, which are of better data quality for evaluating docking tools and scoring functions in existing works. We used the refined set to validate the performance of LigPose with five-fold cross-validation. In each fold, the rest of the samples in the general set with non-overlapping to the validation set are used for training. Performance for 2002 selected complexes in the refined set as adopted in [10] under a similar setting is also reported. For the core set we obtain the training data following the previous deep learning-based methods, *e.g.*, DeepDock[12], RTMScore[36].

The peptide-like SOMs are identified by the Biologically Interesting Molecule Reference Dictionary (BIRD)[80]. 2200 random selected samples in the training set are used for hyper-parameter search, and the selected architecture is used for all tasks. The unsuccessfully processed data by RDKit[81] is removed. None of the samples in the core set but 14 samples in the refined set failed to be processed. Finally, only a minor proportion of the entire PDBbind database (153, < 1%) is dropped.

Auxiliary unlabeled dataset. The structure-determined complexes are only a tiny portion of the complex family. To enhance the performance and generalizability of LigPose, we add a task to LigPose to train it under a self-supervised learning scheme, which models the data structures from large-scale unlabeled data, *i.e.*, with unknown complex structures and protein/ligand properties. To this end, we collected a large unlabelled dataset, including a total number of 2147477 SOMs and 171789 proteins. The SOMs are derived from two databases, *i.e.*, DrugBank[82] (11290) and ChEMBL[83] (2136187), with diversified drug/drug-like compounds that are widely used for the pre-training of SOM features[84]. The proteins are derived from the PDB database[85].

Test dataset. The whole core set and the benchmark dataset CASF-2016[86] derived from the core set with carefully designed poses are used for testing. We adopt four main tasks, *i.e.*, scoring power (the ability to estimate binding affinity), ranking power (the ability to identify near-native pose), docking power (the ability to identify near-native pose), forward screening power (the ability to identify potential ligands for a target protein) and reverse screening power (the ability to identify potential target proteins for a SOM), to comprehensively assess the performance of LigPose. As abovementioned, all complexes in the core set are removed from the training set to make them non-overlapped.

4.1.2 Real-world dataset

To demonstrate the ability of LigPose in real applications, we perform it on two major tasks (*i.e.*, complex structure prediction and screening) for the drug development of SARS-CoV-2 M^{pro}.

M^{pro} structure dataset. We adopt the dataset as reported in [43], which contains 44 non-covalent and non-surface-bound ligands with M^{pro} from SARS-CoV-2.

M^{pro} screening dataset. The screening set ($N = 344$) contains SOM binding data by experimentally measuring the enzymatic activity of M^{pro}, which is collected from DrugCentral[46], followed with a processing protocol introduced in ImageMol[47].

4.2 Pre-processing

In this work, the protein pocket was adopted as the binding target, since obtaining the atomically refined structure is the major concern in drug development[87, 4]. Besides, many methods have been successfully developed to predict the ligand-binding pockets with high accuracies[66, 67, 68, 69, 88, 89].

The protein pockets are the surrounding amino acids of the ligands in 3-D space. For the unlabeled data, we complete the missing atoms with modeler[90] and search the pockets using the Fpocket[91] method with the default setting. All pockets are filtered with a Druggability Score of > 0.5 , therefore, 631687 pockets are finally used. Fpocket recognizes the pocket and represents the pocket center as virtual atoms. A residue is selected as the part of a pocket when its C α atom is within 13Å to the nearest virtual atom. For the labeled data, a residue is selected as the part of a pocket when its C α atom is within 15Å to the nearest ligand atom. Water molecules are not considered in this study.

For a given protein-ligand pair, *i.e.*, a random pair in the unlabeled dataset or a native complex in the PDBbind dataset, a complete undirected graph is firstly constructed using RDKit[81], with each node representing an atom, and all nodes (including themselves) are mutually connected. We initialize the graph by features listed in Suppl. Table A3. In particular, the nodes are initialized as vectors with a length of 79 for a protein and 45 for a ligand, containing the chemical features. Edges are also initialized as vectors with a length of 7 including covalent bond features and distance. Distances connecting different rigid parts are masked with -1 . To enable the ability of SE(3)-equivalence for the method, and also augment the data, we implement a stochastic strategy to initialize the coordinates of the ligands. In this case, the protein nodes are kept in their original positions, while the positions of the ligand nodes are randomly initialized inside the pocket with an empirical distance. In this work, we initialize them in a Gaussian distribution with a standard deviation of 10Å.

4.3 LigPose architecture

LigPose directly predicts the structure of the ligand-binding conformations with their target protein pockets in the 3-D space in an end-to-end manner. As shown in Fig. 1c, LigPose has a graph transformer architecture, with three major components, (1) a sampling and recycling strategy, (2) a feature update block followed by a coordinate update block to forward the features and coordinates through the graph, and the two blocks are stacked 6 times with unshared weights, and (3) a stochastic initialization method for ligand nodes and a novel symmetric-aware loss. We will then illustrate them below.

4.3.1 Sampling and recycling

Typically, a protein pocket contains hundreds of atoms. Using all of them as the input is inefficient and memory unaffordable for common GPU devices. Therefore, we adopt a sampling strategy to generate a sub-graph consisting of all *core atoms* and some randomly selected *context atoms*, with their respective edges, to feed to the network. Specifically, the core atoms involve all ligand atoms, and the $C\alpha$, $C\beta$ atoms of the protein, as they are enough to determine the position and orientation of the amino acids and protein backbone[92, 93]. The other protein atoms are regarded as the context atoms to describe the structural details of the amino acids. Since the nodes are not fully used, we further introduce a recycling strategy, to enhance the representability of the method, as inspired by [17]. In each cycle, a new sub-graph is sampled and forwarded, then, the updated graph is reused in the next cycle. In the next cycle, the newly sampled graph directly inherits the coordinates of corresponding nodes from the last cycle, and its features of the core atoms are combined with the last updated features by using an element-wise gate on the new features, implementing a partial update. (See details in Suppl. Sec. A.2.2)

4.3.2 Feature Update Block

The feature update block maintains a graph Transformer-based architecture to forward the node and edge features. It iteratively performs two operations, *i.e.*, message aggregation and feedforward. In message aggregation, information is aggregated from neighboring nodes to a central node using the multi-head attention (MHA) mechanism (Fig. A3)[94]. In addition, the edge features are also incorporated to enhance the representation.

We use conventional cross-attention to calculate the MHA in the network, according to Query (denote as \mathbf{q}), Key (denote as \mathbf{k}), and Value (denote as \mathbf{v})[94] (See details in Suppl. Sec. A.2.2). Briefly, \mathbf{q} and \mathbf{v} are produced by the features of the central nodes and the neighboring nodes, respectively (see Fig. A3b). \mathbf{k} is extracted from the edge feature and a linearly transformed neighboring node feature (Fig. A3a-b). The edge feature here is enhanced by the spatial information using the distance between the central node and its neighboring node (Fig. A3a). A softmax layer is then applied to the product of \mathbf{q} and \mathbf{k} to get attention masks for each \mathbf{v} . The central node aggregates the

masked \mathbf{v} to get an updated feature, and is followed by a linear layer to merge multi-head information (Fig. A3c). An element-wise gate is implemented on these combined results. Finally, a two-layer multi-layer perceptron (MLP) is applied in the feedforward step and is also enhanced by an element-wise gate. The edge feature is then updated with the element-wise production of \mathbf{q} and \mathbf{k} (Fig. A3d).

4.3.3 Coordinate Update Block

The coordinate update block updates the coordinates of the nodes (atoms) in 3-D space based on the attentions derived from the feature update block, as also introduced in [95] (Fig. A3e-f). To be specific, the attention is transformed to a one-dimensional distance gradient, indicating the change in distance between the central node and each of its neighboring nodes. Then, the coordinate of a certain central node is updated by the sum of these distance gradients calculated with all neighboring nodes, as written by,

$$\Delta_h = \sum_{j \in Neighbor(i)} \frac{\mathbf{x}_i - \mathbf{x}_j}{\|\mathbf{x}_i - \mathbf{x}_j\|_2} \Phi(\mathbf{q}_{ij} \odot \mathbf{k}_{ij}), \quad (1)$$

$$\mathbf{x}'_i = \mathbf{x}_i + \sum_{h=1, \dots, N_h} \lambda_h \Delta_h, \quad (2)$$

where \mathbf{x}_i denote the coordinate of a central node i , \mathbf{x}_j denote the coordinate of a neighbouring node j , \mathbf{q}_{ij} and \mathbf{k}_{ij} are the Query and Key for i and j , respectively, as obtained in the feature update block. The element-wise multiplication (\odot) of \mathbf{q}_{ij} and \mathbf{k}_{ij} are then transformed to a single distance variable by a linear layer Φ , and multiplied by the direction of a central node's coordinate (\mathbf{x}_i) to one of its neighboring node's coordinate (\mathbf{x}_j). The coordinate update Δ_h for node i is then obtained by aggregating Δ for all i 's neighbouring nodes ($Neighbor(i)$), where i is not equal to j . \mathbf{x}_i is then updated by the weighted sum of all Δ_h to \mathbf{x}'_i . Finally, the coordinates were updated using MHA with λ_h weighted N_h heads.

4.4 Correlation-enhanced graph learning

We introduce a novel training paradigm, namely correlation-enhanced biomolecular graph learning, that simultaneously learns both the graph features and the 3D structures for proteins and SOMs. In brief, in each training iteration, the network is trained with a half-to-half chance by a labeled sample (*i.e.*, a native complex) or an unlabeled sample (*i.e.*, a randomly paired protein and ligand). We use the Monte Carlo method to choose one cycle to optimize the network parameters, as also adopted by [17]. Details of the training schedule can be found in Suppl. Sec. A.3

4.4.1 Training with native complexes

Given a ligand containing N_{lig} atoms (nodes). In each iteration, an index is created for mapping the nodes from the predicted pose to the native pose,

ensuring the loss is calculated on atoms with the same chemical identity. Then, the loss for structure prediction is calculated by averaging the differential between the predicted and native ligand coordinates using the atom mapping (denote as \mathcal{L}_{coord}),

$$\mathcal{L}_{coord} = \frac{1}{N_{lig}} \sum_{i \in Nodes(lig)} \|\mathbf{x}_i^{pred} - \mathbf{x}_i^{true}\|_2. \quad (3)$$

where $Nodes(lig)$ denotes the set of all ligand nodes. However, many ligands have symmetric structures. In such cases, multiple equivalent indexes can be created for one ligand (see an example in Suppl. Fig. A4). To solve the problem, we design a specific loss function, *i.e.*, the symmetric-aware loss (denote as \mathcal{L}_{sym}), to update the coordinates, which can be formally written as,

$$\mathcal{L}_{sym} = \min_{sym}(\mathcal{L}_{coord,s}), s \in \{1, \dots, N_s\}. \quad (4)$$

where $\min_{sym}(\cdot)$ calculates the losses for N_s equivalent indexes of the ligand and chooses the minimum one. The final loss for one complex is calculated as a weighted sum of the following three terms: (1) an average of \mathcal{L}_{sym} calculated with the outputs of all coordinate update blocks; (2) a \mathcal{L}_{sym} calculated with the final coordinate prediction in the chosen cycle; and (3) an affinity loss (see Suppl. Methods for details).

4.4.2 Training with randomly paired proteins and ligands

For an unlabeled sample, the loss function (denote as \mathcal{L}_{semi}) consists of two parts, *i.e.*, the Masking-based Complex Modeling (MCM, denote as \mathcal{L}_{mask}) and the Denoising-based Protein structure Reconstruction (DPR, denote as \mathcal{L}_{noise}). Then, \mathcal{L}_{self} can be formally written as,

$$\mathcal{L}_{self} = \mathcal{L}_{mask} + \mathcal{L}_{noise}. \quad (5)$$

These losses are designed to prepare the network parameters in two aspects. First, the MCM loss \mathcal{L}_{mask} is proposed to guide the model to recognize the atom properties. A portion of nodes and edges are masked with a specific token, that encourages the model to predict the original classes of the nodes and edges, as shown in Fig. A5a. Next, the DPR loss \mathcal{L}_{noise} aims to learn representative features for the experimentally solved protein structures, in which random spatial noises are applied to part of the protein nodes, that encourage the model to predict the original position of these nodes, as shown in Fig. A5b.

4.4.3 Training & evaluation for different tasks

CASF-2016. For the screening power, the model starts with the model evaluated on the core set for the structure prediction task, where an additional task is included, *i.e.*, predicting the probability of the SOM to be a true ligand of a protein, to be complementary to the structure prediction task. The

final screen score is obtained by jointly considering this probability and affinity, as the product of these two predictions. With the same training set for the structure prediction task, all proteins and SOMs in PDBbind are paired as positive or negative samples. Proteins with the same UniProt IDs or the same protein names share the same positive SOMs, and SOMs with the same 3-letter PDB IDs share the same positive proteins. The rest pairs are labeled as negative samples. (see Suppl. Methods for details). For the scoring power, we report Pearson R for affinity estimations. For the docking power, we use the LigPose^{score} to identify the near-native pose in the CASF-2016 decoy set. **Structure prediction and virtual screening for M^{Pro}.** We use five-fold cross-validation for structure prediction and virtual screening of M^{Pro}. The training details of LigPose can be found in Suppl. Methods.

4.5 Metrics

The Root Mean Square Deviation (RMSD) value between the predicted and native structures is used to evaluate the structure predictions. The RMSD value of 2Å is widely adopted in related works[10, 86] as a standard to determine the success or failure of the prediction, as also adopted in this work.

The screening power was evaluated on 57 proteins coupled with 285 SOMs in CASF-2016. In this dataset, each protein has 5 ligands as true binding cases, then, the rest of the ligands are regarded as negative ones. The performance was assessed by the percentage of best ligands included in 1%, 5%, and 10% of the top-ranked ligands[86], and the best ligand is the ligand of the highest affinity among 5 true ligands for each protein. Besides, the enhancement factor (EF) is also used to assess the ability of screening which was introduced in Ref.[86]. In brief, EF is used to assess the ability to rank the true ligands on the top ranking position which also uses 1%, 5%, and 10% as cutoffs.

4.6 Configurations of docking tools

For docking tools, the ligands were firstly rotated 180° through the Z-axis with their original conformation[10], followed by energy minimization with Open Bable toolbox[96]. The docking sites were determined by the native positions of ligands. The amount of generated poses for a certain ligand was set to 20, as also adopted in other works[13, 10, 15]. The number of CPU cores was set to 1 to calculate the time cost for prediction (*i.e.*, inference time). The outputs were analyzed using RDKit[81]. Settings details of all docking tools are introduced in Suppl. Sec. A.7.

4.7 Data availability

PDBbind (version 2020) and CASF-2016 are available at <http://www.pdbbind.org.cn>. The PDBbind-CrossDocked-Core set is available

at https://github.com/sc8668/ml_pose_prediction. The M^{PRO} complex structure benchmark is available at <https://github.com/shanizev/Benchmarking-SARS-CoV-2>. Experimentally measured enzymatic activity of M^{PRO} is available at NCATS[46] (<https://opendata.ncats.nih.gov/covid19/assays>).

4.8 Code availability

The source code of LigPose is available under an open-source license at <https://gitfront.io/r/LigPose/kMWuV4DW6JpE/LigPose4Review/>.

Supplementary information. This paper accompanies supplementary information in the "Supplementary Material".

Acknowledgments. This work was supported in part by the National Nature Science Foundation of China under Grant No. 62106101. This work was also supported in part by the Natural Science Foundation of Jiangsu Province under Grant No. BK20210180.

Author contributions. K.H. and J.Z. led the research. K.H. and T.D. contributed to the idea and developed the method. T.D. developed data processing and analytics. K.H., T.D., J.W., and J.Z. wrote the paper.

Correspondence and requests for materials. should be addressed to Junfeng Zhang and Jinhui Wu.

Competing interests. The authors declare no competing interests.

Appendix A Supplementary Materials

A.1 Notations

We summarize the notations present in this paper in Table A2.

A.2 Supplementary Methods

LigPose consists of three key components (see main text Fig. 1d), 1) a sampling and recycling strategy, 2) a stochastic coordinate initialization combined with a symmetric-aware loss function, and 3) a multi-task training scheme including the self-supervised learning on large-scale unlabeled data. The implementation details of these components will be introduced below.

A.2.1 Sampling and recycling

To reduce the computational burden of handling a large number of protein atoms, we proposed a sampling strategy for protein atoms. Specifically, for a given graph representing a protein-ligand pair, a sub-graph including all ligand atoms, and the $C\alpha$ and $C\beta$ atoms derived from the protein pocket, is used to feed the model. These atoms are denoted as *core atoms*. Then, a set of atoms that are randomly sampled from the rest of the protein pocket atoms (denote as *context atoms*), are also included in the graph. The total number of core and context atoms are denoted as N_{total} . All edges are assigned according to the real inter-atom relationship. Since the atoms of the complex are not fully used, which may weaken the representative ability of the method, we introduce a recycling strategy to compensate for it. In this case, the method is processed cycles for one complex, and within each cycle, the features and the coordinates of the complex are updated N_l times using the stacked feature and coordinate update blocks. Besides, in each cycle except the first cycle, the last updated features of the core atoms will be added to a newly sampled sub-graph with the same Ψ as defined in the feature update block, while the last updated features of the context atoms are ignored, to conduct a "partial update". The edge features are updated with the same principle. And the coordinates of the ligand nodes in the newly sampled sub-graph are directly assigned with their last updated values. Then, the sub-graph will be fed to the model again. The recycling will be performed N_c times ($N_c = 4$ in this work).

A.2.2 Feature update block

The feature update block extracts features of all nodes with an architecture based on Graph Transformer[97, 98]. Given an input graph $G = (V, E)$, the feature of the i th node $\mathbf{f}_i \in V$, and the feature of the edge between the i th node and its j th neighbouring node (denote as $\mathbf{e}_{ij} \in E$) are initialized as \mathbf{f}_i^{init} and \mathbf{e}_{ij}^{init} , respectively, according to Table A3. Then, each feature is fed to a linear layer with respect to its feature type (*i.e.*, the protein node feature, the ligand node feature, and the edge feature). The output features of the nodes

(denoted as \mathbf{f}_i^0) are in the same size d_f . The output features of the edges are denoted as \mathbf{e}_{ij}^0 with the size of d_e .

The features are then processed by the number of $N_l = 6$ feature-and-coordinate update blocks. The feature update block conducts two operations, *i.e.*, message aggregation and feedforward. For a message aggregation step in the $l \in \{1, \dots, N_l\}$ th block, the central nodes aggregate the information from the neighboring nodes using both their features and coordinates. In particular, we calculate the Query (denote as \mathbf{q}), Key (denote as \mathbf{k}) and Value (denote as \mathbf{v}) in the block, as written by,

$$\mathbf{d}_{ij}^l = \text{Concat}(\text{RBF}(\|\mathbf{x}_i^{l-1} - \mathbf{x}_j^{l-1}\|_2), \mathbf{e}_{ij}^{l-1}), \quad (\text{A1})$$

$$\mathbf{k}_j^{h,l} = \mathbf{W}_k^{h,l} \mathbf{f}_j^{l-1} \odot \text{LeakyReLU}(\mathbf{W}_e^{h,l} \mathbf{d}_{ij}^l), \quad (\text{A2})$$

$$\mathbf{q}_i^{h,l} = \mathbf{W}_q^{h,l} \mathbf{f}_i^{l-1}, \quad (\text{A3})$$

$$\mathbf{v}_j^{h,l} = \mathbf{W}_v^{h,l} \mathbf{f}_j^{l-1}, \quad (\text{A4})$$

where \mathbf{x}_i^{l-1} and \mathbf{x}_j^{l-1} denote the output coordinates of the i th central node and its j th neighboring node of the $l - 1$ th block, respectively. In the rest of Supplementary Materials, \mathbf{W} denote the learnable parameters of Linear layers, and their biases are omitted for simplicity, where $\mathbf{W}_e^l \in \mathbb{R}^{d_h \times (d_e + d_r)}$, $\mathbf{W}_q^{h,l}, \mathbf{W}_k^{h,l}, \mathbf{W}_v^{h,l} \in \mathbb{R}^{d_h \times d_f}$. $\text{Concat}(\cdot)$ denotes the concatenation operation. The Radial Basis Function (RBF) is used to encode the spatial information of coordinates, resulting in d_r dimensions. d_h denote the dimension of the h th ($h \in \{1, \dots, N_h\}$) attention head. In this work, $d_h = d_f / N_h$. \odot stands for element-wise multiplication.

The output of the message aggregation is then calculated by the following steps,

$$\mathbf{a}_{ij}^{h,l} = \mathbf{q}_i^{h,l} \odot \mathbf{k}_j^{h,l}, \quad (\text{A5})$$

$$\omega_{ij}^{h,l} = \text{softmax}_j\left(\frac{1}{\sqrt{d_h}} \mathbf{a}_{ij}^{h,l} \mathbf{1}\right), \quad (\text{A6})$$

$$\hat{\mathbf{f}}_i^l = \mathbf{W}_{f,o}^l \text{Concat}\left(\sum_{j \in \text{Neighbor}(i)} \omega_{ij}^{h,l} \text{Concat}(\mathbf{v}_i^{h,l}, \mathbf{v}_j^{h,l})\right), \quad (\text{A7})$$

$$\hat{\mathbf{e}}_{ij}^l = \mathbf{W}_{e,o}^l \text{Concat}\left(\omega_{ij}^{h,l} \text{LeakyReLU}(\mathbf{W}_t^{h,l} \mathbf{d}_{ij}^l)\right), \quad (\text{A8})$$

where $\mathbf{W}_{f,o}^{h,l} \in \mathbb{R}^{d_f \times 2d_f}$, $\mathbf{W}_{e,o}^{h,l} \in \mathbb{R}^{d_e \times d_f}$, $\mathbf{W}_t^l \in \mathbb{R}^{d_h \times (d_e + d_r)}$. $\text{Neighbor}(i)$ denote the set of neighboring nodes of the i th central node.

Before feeding the node and edge features to the feedforward step in l th block, we apply a novel proposed element-wise gate $\Psi(\cdot)$ on them, as inspired by [98]. The gated output of the node feature $\hat{\mathbf{f}}_i^l$ can be written as,

$$\mathbf{g}^l = \text{sigmoid}(\mathbf{W}_g^l \text{Concat}(\hat{\mathbf{f}}_i^l, \mathbf{f}_i^{l-1}, \hat{\mathbf{f}}_i^l - \mathbf{f}_i^{l-1})), \quad (\text{A9})$$

$$\hat{\mathbf{f}}_i^l = \Psi_{f,1}^l(\hat{\mathbf{f}}_i^l, \mathbf{f}_i^{l-1}) = \text{Norm}(\mathbf{g}^l \odot \hat{\mathbf{f}}_i^l + \mathbf{f}_i^{l-1}), \quad (\text{A10})$$

where $\mathbf{W}_g \in \mathbb{R}^{d_f \times 3d_f}$, $\text{Norm}(\cdot)$ denote the Layer Normalization[99], and \mathbf{f}_i^l is the final updated features in the l th block. $\hat{\mathbf{f}}_i^l$ is then fed to the feedforward step, as calculated by,

$$\mathbf{f}_i^l = \Psi_{f,2}^l(\mathbf{W}_{f,2}^l \text{LeakyReLU}(\mathbf{W}_{f,1}^l \hat{\mathbf{f}}_i^l), \hat{\mathbf{f}}_i^l) \quad (\text{A11})$$

where $\mathbf{W}_{f,1}^l, \mathbf{W}_{f,2}^l \in \mathbb{R}^{d_f \times d_f}$. The edge feature \mathbf{e}_{ij}^l is calculated similarly.

A.2.3 Coordinate update block

The coordinate update block updates the coordinate of the nodes (atoms) in 3-D space along with the feature update block, as inspired by [95]. Specifically, for the l th block, the coordinates are updated as follows,

$$\Delta_h^l = \sum_{j \in \text{Neighbor}(i)} \frac{\mathbf{x}_i^{l-1} - \mathbf{x}_j^{l-1}}{\|\mathbf{x}_i^{l-1} - \mathbf{x}_j^{l-1}\|_2} \mathbf{W}_x^l \mathbf{a}_{ij}^{h,l}, \quad (\text{A12})$$

$$\mathbf{x}_i^l = \mathbf{x}_i^{l-1} + \sum_{h \in 1, \dots, N_h} \lambda_h^l \Delta_h^l, \quad (\text{A13})$$

where $\mathbf{a}_{ij}^{h,l}$ is calculated in the feature update block (refer to Eq. A5), \mathbf{x} denote the coordinate, $\mathbf{W}_x^l \in \mathbb{R}^{l \times d_h}$. Note that only the coordinates of the ligand nodes are updated.

A.2.4 Affinity prediction and virtual screening

LigPose maintains a multi-task learning framework to simultaneously predict the structure, affinity score, and binding power. Thus, it also estimates the affinity of the protein-ligand complex as the auxiliary task, to be complementary to the coordinate prediction. In this case, the pooled node features $\mathbf{f}_i^{N_i}$ and edge features $\mathbf{e}_j^{N_e}$ are fed to a two-layer multi-layer perceptron, as calculated by,

$$\mathbf{r} = \text{Norm}(\text{Concat}(\frac{1}{N_f} \sum_{i \in 1, \dots, N_f} \mathbf{f}_i^{N_i}, \frac{1}{N_e} \sum_{j \in 1, \dots, N_e} \mathbf{e}_j^{N_e})) \quad (\text{A14})$$

$$\mathbf{y}_{aff} = \text{ReLU}(\mathbf{W}_{a,2} \text{LeakyReLU}(\mathbf{W}_{a,1} \mathbf{r})), \quad (\text{A15})$$

where \mathbf{y}_{aff} denote the prediction of the affinity, $\mathbf{W}_{a,1} \in \mathbb{R}^{(d_f+d_e) \times (d_f+d_e)}$, $\mathbf{W}_{a,2} \in \mathbb{R}^{1 \times (d_f+d_e)}$, and N_f, N_e denotes the number of nodes and edges, respectively.

To screen the possible drugs, we provide a probability estimation (denoted as \mathbf{y}_{bind}) to indicate whether a SOM binds to a protein. The probability estimation also served as an additional task, similar to the affinity estimation task, with the ReLU layer replaced by the Sigmoid layer.

A.3 Training

A.3.1 Correlation-enhanced graph learning

Training with native complexes

Two losses are used in the training stage, *i.e.*, the symmetric-aware loss for structure prediction (as introduced in 4.2), and the affinity loss for binding affinity prediction. The affinities are collected by PDBbind, including *Ki*, *Kd*, and *IC50*. Their negative log scale is used for training and evaluation. Then, the affinity loss is predicted for each protein-ligand pair, as defined by,

$$\mathcal{L}_{aff} = \|\mathbf{y}_{aff}^{pred} - \mathbf{y}_{aff}^{true}\|_2^2. \quad (\text{A16})$$

Then, the final loss of the network is defined as,

$$\mathcal{L} = \gamma_1 \left(\frac{1}{N_l - 2} \sum_{l \in \{2, \dots, N_l - 1\}} \mathcal{L}_{sym}^l + \mathcal{L}_{sym}^{N_l} \right) + \gamma_2 \mathcal{L}_{aff}, \quad (\text{A17})$$

where \mathcal{L}_{sym} is the proposed symmetric-aware loss calculated with coordinate output with the new N_l blocks as defined in the main text (refer to Main Text Eq. 4) and the equivalent indexes used for \mathcal{L}_{sym} are obtained from RDKit[81]. γ_1 and γ_2 are weight parameters to balance the losses.

We adopt a two-step training schedule. The first step limits the maximum number of nodes to 200, then the second step increases this number. The full training schedule is listed in Table A6.

2200 random samples in the training set (when testing on the core set) are used to tune the hyper-parameters of the backbone of LigPose^{light} without training with unlabeled data. The search space is shown in Table A5. For LigPose, we simply increase the complexity of it on hidden size, number of cycling, and number of max nodes. The chosen architectures are shown in Table A4. We used the Adam optimizer with an exponentially decayed learning rate, with a decay rate of 0.99. Besides, all coordinates and affinities are rescaled to 1/10 of their original values for stable training. And these hyper-parameters are preserved in all downstream tasks.

Training with randomly paired proteins and ligands

Learning on the unlabeled data aims to encourage the model to learn graph features and biomolecular atom correlations simultaneously via self-supervised learning. The entire self-supervised learning loss function (denote as \mathcal{L}_{self}) consists of two parts, *i.e.*, the Masking-based Complex Modeling (MCM, denote as \mathcal{L}_{mask}) and the Denoising-based Protein structure Reconstruction (DPR, denote as \mathcal{L}_{noise}). Also, to further generalize the model to very strict conditions of non-similar seen molecules, we pre-trained LigPose with docking-based structures (see Sec. A.9.5).

Masking-based complex modeling (MCM). In a molecular graph, the attribute of a node can be inferred from the contextual nodes and edges[100]. Therefore, we train the network by masking part of the nodes and edges in a protein-ligand pair with a specific token [MASK], *i.e.*, the original features

are zeros after masked. The masking ratio is 15% for both nodes and edges. This MCM stage encourages the network to learn distinct atom features for the proteins and SOMs. The output features of the node $\mathbf{f}_i^{N_i}$ and the edge $\mathbf{e}_j^{N_i}$ followed by a two-layer MLP are then used to predict their true identical attributes, *i.e.*, the element types of SOM nodes (denote as $\mathcal{L}_{mask}^{l_elem_type}$), the atom and residue types of protein nodes (denote as $\mathcal{L}_{mask}^{p_atom_type}$ and $\mathcal{L}_{mask}^{p_res_type}$). For the edges, the network is trained to predict their bond types (denote as $\mathcal{L}_{mask}^{bond_type}$). The protein-SOM edges are excluded in this MFP stage. Notably, masking is performed in both directions for edges, *i.e.*, the two edges connected same nodes are masked together. If an atom type involves symmetry, only one of them will be preserved (*e.g.*, *CG1* and *CG2* atoms in valine). Additionally, the distance features involved in masking will not be masked. At least one protein node, one SOM node, two protein edges, and two SOM edges are masked in each iteration. We use the Focal loss[101] to calculate the loss. The final \mathcal{L}_{mask} are weighted as:

$$\mathcal{L}_{mask} = \mathcal{L}_{mask}^{p_atom_type} + \mathcal{L}_{mask}^{p_res_type} + \mathcal{L}_{mask}^{l_elem_type} + \mathcal{L}_{mask}^{bond_type} \quad (\text{A18})$$

Denoising-based protein structure reconstruction (DPR). This strategy encourages the model to reconstruct the original protein structure when spatial noises are applied to the protein nodes. Specifically, a random position noise ($noise \sim N(0, \sigma^2)$, $\sigma = 2\text{\AA}$) is applied. To calculate the loss, the average distance between the denoised position and the real position is calculated. In this work, the noisy protein nodes are randomly sampled in each iteration, with a sampling ratio the same as the masking rate.

A.3.2 Downstream tasks

Affinity estimation

We perform post-training of 3 epochs for LigPose, with higher loss weight for affinity. The training schedule is listed in Table A7.

Virtual screening on CASF-2016

We train the model for virtual screening using Focal loss[101] with a weight γ_3 after the training of the structure prediction task. The model predicts the probability of a SOM to be a true ligand for a certain protein, as described in 4.4.3. In each training iteration, we balance the positive and negative pairs to be equally presented. Please note that all pairs containing data from the core set are not used for training. Also, \mathcal{L}_{sym} and \mathcal{L}_{aff} are used if the native complex structures and affinities can be provided. The specific hyper-parameter setting for virtual screening is shown in Table A7, while the others are the same as the structure prediction task. The training schedule is listed in Table A7.

Structure prediction for M^{pro}-ligand complex

We train the LigPose with similar settings as described in Sec. A.3.1 with 11 structures of SARS-CoV and MERS-CoV collected from PDB. The training schedule is listed in Table A7.

Virtual screening on M^{pro} enzymatic activity

We perform five-fold cross-validation to the M^{pro} enzymatic activity data. The training process is similar to CASF-2016. The M^{pro} structures randomly paired with SOMs are used as the inputs. The training schedule is listed in Table A7. For ImageMol, starting with its pre-trained weights, we adopt a set of fine-tuning parameters suggested in ImageMol work[47]

A.4 Evaluation

In evaluation, we use an ensemble strategy for LigPose, *i.e.*, predicting $N_{ens} = 10$ times for a given complex.

A.5 Settings for ablation study

We perform an ablation study for LigPose by evaluating the success rate on the core set. We report the performance after removing the corresponding part in the Table. A9.

A.6 Settings for energy minimization

We perform a constraint energy minimization with Merck Molecular Force Field[102] in RDKit[81], with the *maxIters*=20 and *forceConstant*=100.

A.7 Settings for docking tools

The basic settings (*e.g.*, number of generated poses) for all docking tools are introduced in Sec.4.6. Here, we describe the detailed settings below.

Smina All proteins and ligands were converted to *pdbqt* files as described in [103]. The docking sites of the ligands were set by an automatic box creation tool[29] using their native poses. The rest of the parameters were set by default.

LeDock The input files were automatically generated by Lepro[104], including adding hydrogens and defining binding pockets. The rest input parameters are set to default.

AutoDock All proteins and ligands were converted to *pdbqt* files with the same method as Smina. Grid maps were calculated by autogrid4 with default settings. The rest input parameters are set to default.

rDock We adopted a standard docking protocol introduced in Ref.[10] with a system definition file provided in the guidance of rDock.

A.8 Investigation of the protein-ligand interaction

Non-covalent interactions between proteins and ligands were recognized by PLIP[105], including water bridge, hydrophobic interaction, salt bridge, π -cation, hydrogen bond, π -stack, and halogen bond. To better assess the non-covalent interactions between the predicted and native poses, we define the interaction reproducibility similar to[48], as written by,

$$\text{Interaction reproducibility} = \frac{1 + \text{number of shared interactions}}{2 + \text{total number of unique interactions}}. \quad (\text{A19})$$

The predicted ligands were placed in the original *pdb* file and then processed by PLIP to calculate a score of interaction reproducibility. Specifically, the interactions were calculated at the atom level for ligands and the residue level for proteins.

The visualization of attention weights for a single head was analyzed with the non-covalent interactions derived from true ligand pose, and the weight of each protein residue was calculated by the average attention weight of C α nodes.

A.9 Supplementary results

A.9.1 Using as a scoring function

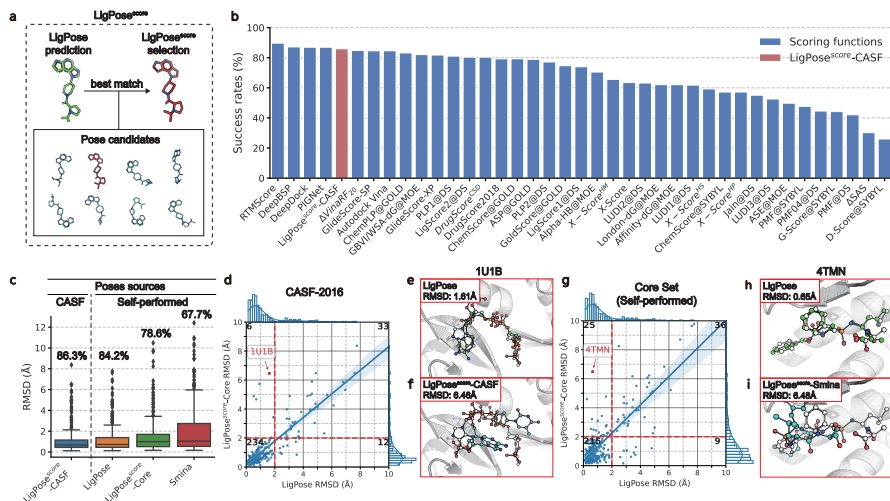


Fig. A1 LigPose used as a scoring function. (a) Brief illustration of LigPose^{score}, which simply chooses a pose candidate that best matches the prediction of LigPose as the top-scored pose. (b) Comparison of success rates between LigPose^{score}-CASF, and 38 well-established scoring functions on CASF-2016 benchmark. (c) RMSD distribution and success rate of Smina, LigPose, and LigPose^{score}-Core, and LigPose^{score}-CASF. (d,g) Correlation plots of RMSD between predictions of LigPose and LigPose^{score} on CASF-2016 (d) and self-performed poses (g), respectively. Each of the figures is partitioned into four regions by two red dashed lines at RMSD of 2Å, with the sample count marked in the corner. (e,f,h,i) Visualization of two representative samples as pointed out in d and g. Prediction of LigPose (e,h), LigPose^{score} (f,i), and the native poses (e,f,h,i) are denoted as green, cyan and white color, respectively. The oxygen and nitrogen atoms are denoted as red and blue color, respectively.

Other than directly predicting the poses, we show an extended application of LigPose, *i.e.*, treating it as a scoring function to build LigPose^{score}, by choosing the pose candidate that best matches the prediction of LigPose using the metric of RMSD (see a brief illustration in Fig. A1a). Thus, LigPose^{score} can be composed with docking and evaluated on the Comparative Assessment of Scoring Functions (CASF-2016) benchmark[86] derived from the core set. The benchmark is carefully designed to evaluate the capacity of scoring functions, with pose candidates being the clustering centers of docking sampled poses, using RMSD and conformation similarity as the clustering index.

As suggested by Fig. A1b, our method (denote as LigPose^{score}-CASF) with a success rate of 86.3% outperformed 34 conventional scoring functions (with success rates ranging from 26.0% to 84.9%), and was also comparable to the state-of-the-art deep learning-based scoring functions, *i.e.*, RTM-Score (89.7%)[36], DeepBSP (87.2%)[14], DeepDock (87.0%)[12], and PIGNet

(87.0%)[41]. We conclude the slightly lower performance of LigPose^{score} for two reasons. First, LigPose^{score} still needs to generate a near-native pose, instead of explicitly scoring and ranking the pose candidates, which improves the difficulty of the task. Second, the CASF-2016 benchmark is inadequate to assess the structure prediction ability for real production purposes. Since the RMSD is inaccessible in real-world applications, the native complex structure could not be predetermined during virtual measurement. As previously discussed for Fig. 2e, several works use self-performed poses to partially solve the problem. We adopt this setting and evaluate LigPose^{score} on self-performed poses, by performing Smina on the core set (denote as LigPose^{score}-Core). The RMSD distribution of Smina, LigPose^{score}-Core, and LigPose are shown in Fig. A1c, with LigPose^{score}-CASF as the baseline. As shown in Fig. 2d and Fig. A1c, without selective poses, the success rates of all methods are decreased compared with those in CASF-2016, ranging from 55.1% to 84.2%. LigPose^{score}-Core showed a greatly improved success rate (78.6%) compared with Smina (67.7%) and was also comparable to the best performing scoring function (*i.e.*, RTMScore (80.7%)[36]). Moreover, LigPose (84.2%) outperformed RTMScore and LigPose^{score}-Core with notable higher success rates of 3.5% and 5.6%, respectively, indicating that the end-to-end learning paradigm of LigPose is more effective in real applications without pre-designing the pose candidates.

Furthermore, we plotted the correlation of RMSD in Fig. A1, between LigPose and LigPose^{score}-CASF (d) / -Core (g), each with a typical sample visualized by the predicted structures aside (e,f,h,i). We observed from the figure that docking may mislead the model. For some cases that were correctly predicted by LigPose (*i.e.*, with RMSD < 2Å), LigPose^{score} reshaped them to wrong structures, especially on self-performed poses (with more samples in the upper-left regions in g compared with d). These results also indicate that docking-based sampling and scoring have inevitably ignored limitations for structure prediction in real practice.

A.9.2 Affinity estimation

To further investigate the scalability of LigPose, we also apply it to the task of protein-ligand affinity estimation (denote as LigPose^{affinity}), another core function of docking. For disease-related proteins, ligands with strong binding interactions (*i.e.*, affinity) can be selected as drug candidates. LigPose is feasible to adapt to this task without leveraging native complex structures, by simply adding several task-specific output layers (see Suppl. Sec. A.2.4 for details). The comparisons of LigPose^{affinity} with several recent structure-based deep learning methods[108, 110, 106, 107, 112, 109, 111] on affinity estimation are summarized in Table A1, where LigPose^{affinity} achieved the best performance among the competing methods which do not use native structures, with mean absolute error (MAE) of 0.908, root mean square error (RMSE) of 1.121 and Pearson *R* of 0.834. Compared to the methods that use native structures, LigPose^{affinity} is also comparable or better than the best-performing method

Table A1 Performance comparison for affinity estimation on the core set of PDBbind. Methods that require native complex structures were listed in the second set of rows. Methods without using the native complex structures were listed in the last set of rows. The term "Native" indicates the methods that use the native complex structures for affinity estimation, "Docking" indicates they use the docking-sampled complex structures, and "None" indicates they use none of the above complex structures.

Models	MAE	RMSE	Pearson R	Using Complex Structure		
				Native	Docked	None
Pafnucy[106]	1.13	1.42	0.78	✓		
TopologyNet[107]	-	1.34	0.81	✓		
FAST[108]	1.019	1.308	0.810	✓		
OnionNet[109]	0.984	1.278	0.816	✓		
InteractionGraphNet[110]	0.940	1.220	0.837	✓		
PointTransformer[111]	0.91	1.19	0.852	✓		
FAST[108]	1.498	1.871	0.712		✓	
OnionNet[109]	-	1.523	0.755		✓	
InteractionGraphNet[110]	1.150	1.503	0.757		✓	
APMNet[112]	0.998	1.268	0.815			✓
LigPose ^{affinity}	0.908	1.121	0.834			✓

PointTransformer (MAE: 0.91, RMSE: 1.19, Pearson R : 0.852), indicating its strong ability to learn native-like atom interactions. Therefore, without using native complex structures, LigPose^{affinity} can achieve impressive results that largely outperform other methods.

A.9.3 Ablation study

As reported in Table A9, the performance of LigPose decreases after removing our core designs. The cycling and sampling strategy has the greatest impact on the LigPose, making the success rate drop 16.14%. The rest designs (self-supervised learning, ensemble, and symmetric mapping) show drops in a range of 1.40% to 3.16%.

A.9.4 Accuracy for unseen bio-compounds

We report accuracy after removing ligands in the test set according to Tanimoto similarities[44] to the training set with different cutoffs. As shown in Table A10, the success rate drops by 2.25%–5.92% with the similarity cutoff of 0.70–1.00, which is an acceptable performance for mining unseen compounds.

A.9.5 Accuracy for similarity-based filtering

Here, we investigate the impact of similarity by applying similarity-based filtering for both protein and ligand. The training set is filtered according to its protein and ligand similarity to the test set. As shown in Table A11, LigPose^{light} achieves success rate of 78.60% without similarity filtering (*i.e.* similarity cutoff = 1.0). The success rate drops to 19.30% after filtering

all complex structures with protein or ligand similar to the test set (similarity cutoff = 0.4).

We proposed the docking-based pre-training strategy to leverage the docking-generated structures as the ground-truths for training. This expands the learned chemical space for the model. Then, the models are trained with a selected training set, and the re-docked structures on the test set. We consider two ways to use re-docked structures, *i.e.*, training with top-scored re-docked structures using, and training with the nearest re-docked structures. As shown in Table A11, the success rate of the model increased from 19.30% to 37.89% (nearest) and 56.84% (top-scored), which allowed the model to fit the hardest condition.

It is quite typical for ML/DL-based method's performance to drop significantly when similarity-based filtering is used. For example, DiffDock also does much worse in such strict evaluation context[113]. The primary concern for this comes from the vast chemical space for the combination of protein and ligand. The current experimentally solved structures are limited. For example, the PDBbind (v2020) data set ($N = 19443$) can not afford sufficient samples to generalize the prediction to low-similarity structures.

A.9.6 Energy minimization

We perform energy minimization to ensure the predicted structures are physically plausible. The success rate shows a slight drop of 1.40%, which indicates that the accuracy is dominantly determined by LigPose, and the energy minimization has little impact on the final predictions.

A.9.7 Training time

The product model was trained on 3 NVIDIA A100 GPU devices for about 9 days.

A.10 Supplementary tables

A.11 Protein and ligand similarity

The protein similarity is calculated by the sequence identity using the Needleman-Wunsch algorithm[114]. The ligand similarity is measured using the Tanimoto similarity calculated by Morgan fingerprints[115].

Table A2 Notations.

Notations	Descriptions
N_l	Number of blocks
N_{ens}	Number of ensemble
N_c	Number of cycles
N_h	Number of attention heads
N_f	Number of nodes
N_{lig}	Number of ligand nodes
N_s	Number of ligand equivalent indexes
l	Index of blocks
h	Index of heads
d_f	Dimension of node feature
d_e	Dimension of edge feature
d_h	Dimension of attention head
d_r	Dimension of RBF encoded spacial information
γ_1	Weight for symmetric-aware loss
γ_2	Weight for affinity loss
f	Node feature
e	Edge feature
x	Node coordinate
q	Query for attention
k	Key for attention
v	Value for attention
Δ	Distance gradient
λ	Weight parameter for multi-head attention in coordinate update
\mathcal{L}	Total loss
\mathcal{L}_{coord}	Coordinate loss
\mathcal{L}_{sym}	Symmetric-aware loss
\mathcal{L}_{aff}	Affinity loss
W	Weight parameter of Linear layer
1	Column vector of 1s

Table A3 Feature list of nodes and edges. All features are processed with one-hot encoding except the distances. The initialization of distances is described in the Main text Methods. The feature sizes are denoted in brackets.

Node features		Edge features
Protein node	Ligand node	
element type (4)	element type (10)	covalent connection (1)
atom degree (5)	atom degree (6)	distance (1)
implicit valence (5)	implicit valence (5)	covalent bond type (5)
neighboring H atoms (5)	neighboring H atoms (5)	
atom hybridization (3)	atom hybridization (6)	
amino acid type (20)	formal charge (6)	
atom name (37)	ring of size (6)	
	aromatic type (1)	

Table A4 Hyperparameters for LigPose architecture.

Hyperparameters	LigPose	LigPose ^{light}
Number of feature update blocks	6	6
Number of coordinate update blocks	6	6
Dimension of node feature (d_f)	768	160
Dimension of edge feature (d_e)	384	80
Number of attention heads (N_h)	8	4
Number of ensemble (N_{ens})	10	10
Number of cycles (N_c)	4	3

Table A5 Hyperparameter search space.

Hyperparameters	Search space
Learning rate	$\{1 \times 10^{-3}, 1 \times 10^{-4}, 1 \times 10^{-5}\}$
MHA heads	$\{1, 4, 8\}$
Blocks	$\{3, 6\}$
Node/edge hidden size	$\{160/80, 80/40\}$
Cycles	$\{1, 2, 3, 4\}$

Table A6 Training schedules for structure prediction with PDBbind dataset.

Tasks	Evaluation on core set			Evaluation on refined set	
	Stage 1	Stage 2	Stage 3	Stage 1	Stage 2
Training with additional unlabeled data	✓	✓	✓	×	×
Learning rate	1×10^{-4}	1×10^{-5}	1×10^{-5}	1×10^{-4}	1×10^{-5}
Weight for symmetric-aware loss (γ_1)	1.0	1.0	1.0	1.0	1.0
Weight for affinity loss (γ_2)	1.0	1.0	1.0	1.0	1.0
Batch size	15	3	1	12	4
Epochs	75	5	3	200	3
Number of max nodes	200	440	700	500	700
Model version	<i>c1</i>	<i>c2</i>	<i>c3</i>	<i>r1</i>	<i>r2</i>
Parameters initialized from	Random	<i>c1</i>	<i>c1</i>	Random	<i>r1</i>

Table A7 Training schedules for downstream tasks. The parameter represented by "-" is not used in the corresponding task due to the lack of available data.

Tasks	Affinity estimation	Virtual screening on CASP-2016		Structure prediction for M ^{Pro}	Virtual screening for M ^{Pro}
	Stage 1	Stage 1	Stage 2	Stage 1	Stage 1
Training with additional unlabeled data	✓	×	×	✓	✓
Learning rate	3×10^{-6}	1×10^{-5}	5×10^{-6}	1×10^{-5}	1×10^{-5}
Learning rate decay	0.90	0.99	0.99	0.99	0.90
Weight decay	0	0	0	0	1×10^{-3}
Weight for symmetric-aware loss (γ_1)	0.1	0.2	0.2	1.0	-
Weight for affinity loss (γ_2)	10.0	1.0	1.0	-	-
Weight for virtual screening loss (γ_3)	-	1.0	1.0	-	1.0
Batch size	3	15	3	1	3
Epochs	3	50	30	20	15
Number of max nodes	440	200	440	700	430
Model version	<i>a1</i>	<i>vc1</i>	<i>vc2</i>	<i>m1</i>	<i>vm1</i>
Parameters initialized from	<i>c2</i>	<i>c2</i>	<i>vc1</i>	<i>c3</i>	<i>c2</i>

Table A8 Quantitative comparison of success rate among LigPose, the docking tools, and the hybrid deep learning methods on the PDBbind-CrossDocked-Core set. The upper panel includes three docking tools with their derived hybrid machine/deep learning methods. The best-performed methods are marked in bold.

Methods	Success rates (%)		
	Surflex	Glide	Vina
Docking	43.8	42.2	31.8
Vina	39.8	35.9	32.1
X-Score	41.8	36.2	32.8
Prime-MM/GBSA	42.7	41.0	22.5
NNscore_XGB_Re	47.9	37.6	28.4
NNscore+Rank_XGB_Re	47.8	42.1	33.6
ECIF+Vina_XGB_Re	47.5	41.4	31.2
ECIF+Vina+Rank_XGB_Re	50.1	46.0	36.1
NNscore_XGB_Cross	52.1	44.5	35.2
NNscore+Rank_XGB_Cross	51.7	44.4	35.2
ECIF+Vina_XGB_Cross	50.4	45.3	34.8
ECIF+Vina+Rank_XGB_Cross	52.2	47.1	35.5
DeepDockM	48.0	45.5	37.4
RTMScore	51.9	49.3	40.9
Docking (top 20)	66.7	63.0	51.9
LigPose	72.0		

*Performances of other methods were directly copied from Ref.[36]. The suffix "_Re" indicates training with re-docked poses, and the suffix "_Cross" indicates training with cross-docked poses.

Table A9 Abalation study.

Settings	Success rates (%)
Baseline	84.21
no self-supervised training	81.05
no cycling and sampling	68.07
no ensemble	82.11
no symmetric mapping	82.81

Table A10 Success rates for novel bio-compounds, after removing ligands with different similarity cutoffs in the test set.

Similarity cutoff	LigPose success rates (%)
1.00	84.21
0.95	81.63
0.90	81.96
0.80	80.12
0.70	78.29
0.60	74.12
0.50	71.05
0.40	80.00

Table A11 Success rates on re-docking task for the core set with similarity-based filtered training set.

Protein/ligand similarity cutoffs	Models	Success rates (%)
1.0/1.0	LigPose ^{light}	78.60
0.4/0.4	LigPose ^{light}	19.30
0.4/0.4	LigPose ^{light} + trained with nearest re-docked structures	37.89
0.4/0.4	LigPose ^{light} + trained with top-scored re-docked structures	56.84

A.12 Supplementary figures

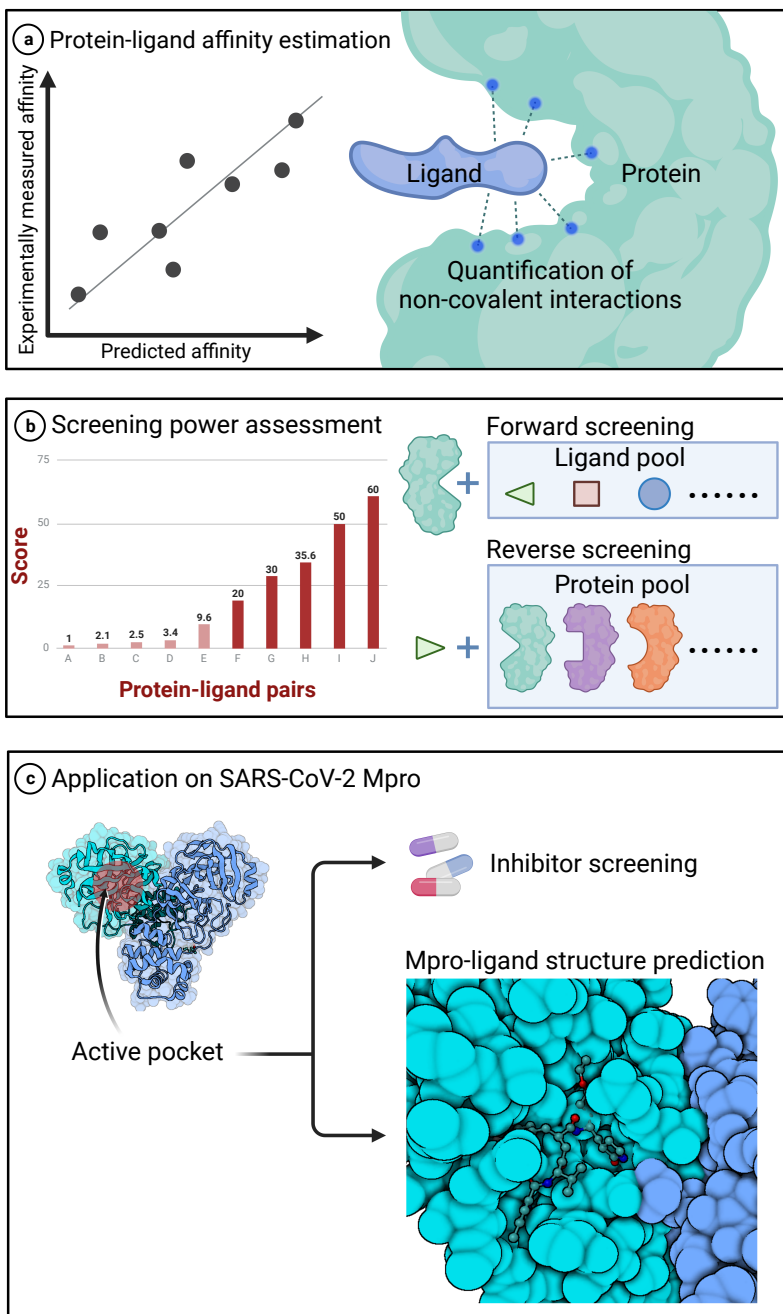


Fig. A2 Multi-task design/evaluation of LigPose in drug development based on accurate structure prediction. (a) Affinity estimation provides strength quantification of protein-ligand interactions. (b) Assessing screening power on forward screening task (*i.e.*, identifying potential binding ligand for a protein) and reverse screening task (*i.e.*, identifying potential binding protein for a SOM). (c) Application of screening and structure prediction for SARS-CoV-2 M^{P_{ro}}.

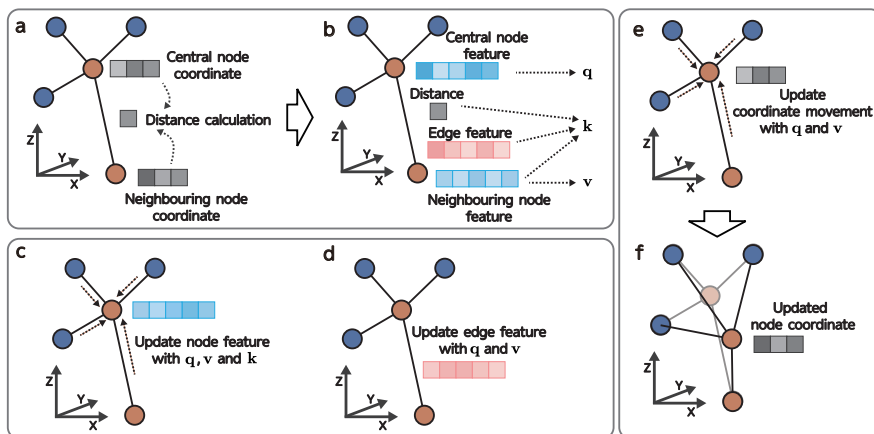


Fig. A3 The updating rules for the nodes and edges of LigPose. (a-f) Updating features of the central node and its related edges by feature update block. (a) Calculating pair-wise distances. (b) Calculating attention weights in feature update block. Arrows show the information flow. (c) Updating central node features with message aggregation. (d) Updating edge features. (e-f) Updating coordinates by coordinate update block. (e) Updating central node coordinates. (f) The updated coordinate of the central node.

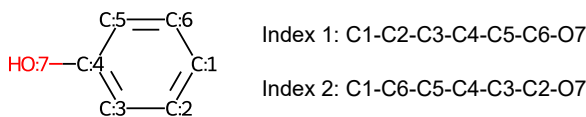


Fig. A4 A symmetric molecule (phenol). Two equivalent indexes, *i.e.*, C1-C2-C3-C4-C5-C6-O7 and C1-C6-C5-C4-C3-C2-O7, can be created for this molecule.

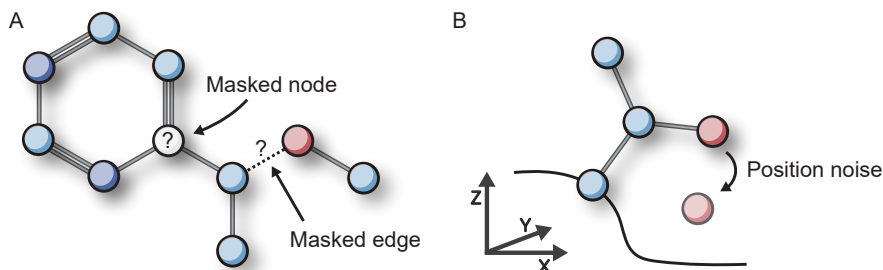


Fig. A5 Schematic of Graph masking and structure denoising of self-supervised learning. a. Nodes or edges are masked, and the model is encouraged to predict their original attributes (*i.e.*, the atom types and bond types). b. Atoms of pockets are noised in 3D spatial, the model is encouraged to reconstruct their positions.

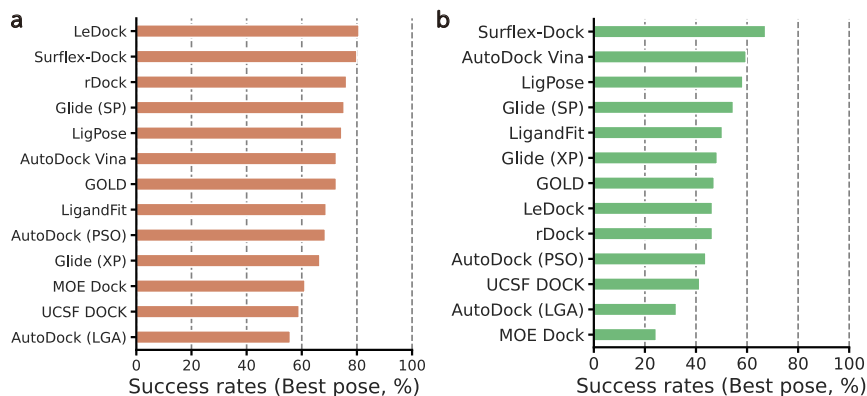


Fig. A6 Quantitative comparison of success rate between LigPose and the best pose generated by docking tools on regular organic (a) or peptide/peptide-like (b) ligands. For regular organic ligands, LeDock achieved the highest success rate of 80.8%. LigPose (success rate of 74.6%) ranked the 5th among all methods. For peptide/peptide-like ligands, Surfex Dock achieved the highest success rate of 67.3%. LigPose (success rate of 58.4%) ranked the 3th among all methods. As described in main text Sec. 2.2, these results can be regarded as the upper bound of docking tools, where LigPose predicts a greatly higher success rate than 8 docking tools.

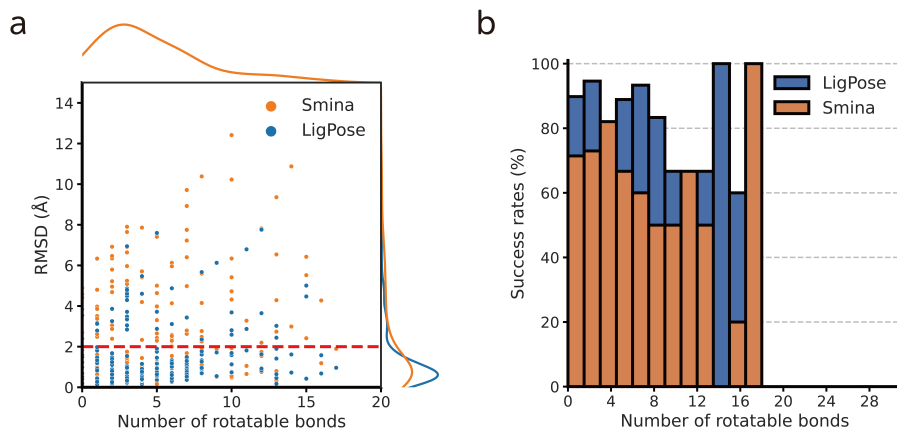


Fig. A7 (a), RMSD values and (b), success rates for prediction of LigPose and Smina with respect to the number of rotatable bonds in the core set of PDBbind. The red dashed line denotes the RMSD threshold of 2Å. LigPose showed better performance in most cases.

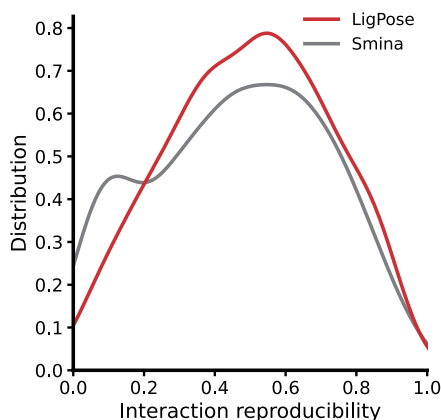


Fig. A8 Distribution of the interaction reproducibility of all non-covalent interactions of LigPose (red line) and Smina (grey line). The higher accuracy of LigPose is positively correlated to better performance on reproducing the native-like non-covalent interactions, which is important for drug screening and lead optimization.

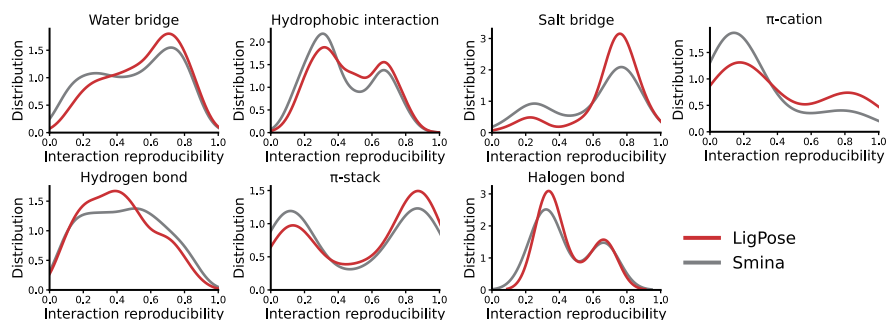


Fig. A9 Distribution of the interaction reproducibility of seven non-covalent interactions of LigPose (red line) and Smina (grey line), including water bridge, hydrophobic interaction, salt bridge, π -cation, hydrogen bond, π -stack and halogen bond. These results indicated that LigPose consistently outperformed Smina on all seven types of non-covalent interactions.

References

- [1] Asher Mullard. 2022 FDA approvals. *Nature reviews. Drug discovery*, 2023.
- [2] Jiankun Lyu, Sheng Wang, Trent E Balius, Isha Singh, Anat Levit, Yurii S Moroz, Matthew J O’Meara, Tao Che, Enkhjargal Alгаа, Kateryna Tolmachova, et al. Ultra-large library docking for discovering new chemotypes. *Nature*, 566(7743):224–229, 2019.
- [3] Mingyue Zheng, Jihui Zhao, Chen Cui, Zunyun Fu, Xutong Li, Xiaohong Liu, Xiaoyu Ding, Xiaoqin Tan, Fei Li, Xiaomin Luo, et al. Computational chemical biology and drug design: Facilitating protein structure, function, and modulation studies. *Medicinal research reviews*, 38(3):914–950, 2018.
- [4] Douglas B Kitchen, H el ene Decornez, John R Furr, and J urgen Bajorath. Docking and scoring in virtual screening for drug discovery: methods and applications. *Nature reviews Drug discovery*, 3(11):935–949, 2004.
- [5] Shengzheng Wang, Guoqiang Dong, and Chunquan Sheng. Structural simplification: an efficient strategy in lead optimization. *Acta Pharmaceutica Sinica B*, 9(5):880–901, 2019.
- [6] Heping Zheng, Katarzyna B Handing, Matthew D Zimmerman, Ivan G Shabalina, Steven C Almo, and Wladek Minor. X-ray crystallography over the past decade for novel drug discovery—where are we heading next? *Expert opinion on drug discovery*, 10(9):975–989, 2015.
- [7] Jean-Paul Renaud, Ashwin Chari, Claudio Ciferri, Wen-ti Liu, Herv e William R emigy, Holger Stark, and Christian Wiesmann. Cryo-EM in drug discovery: achievements, limitations and prospects. *Nature reviews Drug discovery*, 17(7):471–492, 2018.
- [8] Luca Pinzi and Giulio Rastelli. Molecular docking: shifting paradigms in drug discovery. *International journal of molecular sciences*, 20(18):4331, 2019.
- [9] Xuan-Yu Meng, Hong-Xing Zhang, Mihaly Mezei, and Meng Cui. Molecular docking: a powerful approach for structure-based drug discovery. *Current computer-aided drug design*, 7(2):146–157, 2011.
- [10] Zhe Wang, Huiyong Sun, Xiaojun Yao, Dan Li, Lei Xu, Youyong Li, Sheng Tian, and Tingjun Hou. Comprehensive evaluation of ten docking programs on a diverse set of protein–ligand complexes: the prediction accuracy of sampling power and scoring power. *Physical Chemistry Chemical Physics*, 18(18):12964–12975, 2016.
- [11] Dejun Jiang, Chang-Yu Hsieh, Zhenxing Wu, Yu Kang, Jike Wang, Ercheng Wang, Ben Liao, Chao Shen, Lei Xu, Jian Wu, et al. InteractionGraphNet: A novel and efficient deep graph representation learning framework for accurate protein–ligand interaction predictions. *Journal of medicinal chemistry*, 64(24):18209–18232, 2021.
- [12] Oscar M endez-Lucio, Mazen Ahmad, Ehecatl Antonio del Rio-Chanona, and J org Kurt Wegner. A geometric deep learning approach to predict binding conformations of bioactive molecules. *Nature Machine*

- Intelligence*, pages 1–7, 2021.
- [13] Jaechang Lim, Seongok Ryu, Kyubyong Park, Yo Joong Choe, Jiyeon Ham, and Woo Youn Kim. Predicting drug–target interaction using a novel graph neural network with 3D structure-embedded graph representation. *Journal of chemical information and modeling*, 59(9):3981–3988, 2019.
- [14] Jingxiao Bao, Xiao He, and John ZH Zhang. DeepBSP—a machine learning method for accurate prediction of protein–ligand docking structures. *Journal of Chemical Information and Modeling*, 2021.
- [15] Joseph A Morrone, Jeffrey K Weber, Tien Huynh, Heng Luo, and Wendy D Cornell. Combining docking pose rank and structure with deep learning improves protein–ligand binding mode prediction over a baseline docking approach. *Journal of chemical information and modeling*, 60(9):4170–4179, 2020.
- [16] Matthew Ragoza, Joshua Hochuli, Elisa Idrobo, Jocelyn Sunseri, and David Ryan Koes. Protein–ligand scoring with convolutional neural networks. *Journal of chemical information and modeling*, 57(4):942–957, 2017.
- [17] John Jumper, Richard Evans, Alexander Pritzel, Tim Green, Michael Figurnov, Olaf Ronneberger, Kathryn Tunyasuvunakool, Russ Bates, Augustin Židek, Anna Potapenko, et al. Highly accurate protein structure prediction with AlphaFold. *Nature*, 596(7873):583–589, 2021.
- [18] Minkyung Baek, Frank DiMaio, Ivan Anishchenko, Justas Dauparas, Sergey Ovchinnikov, Gyu Rie Lee, Jue Wang, Qian Cong, Lisa N Kinch, R Dustin Schaeffer, et al. Accurate prediction of protein structures and interactions using a three-track neural network. *Science*, 373(6557):871–876, 2021.
- [19] Zeming Lin, Halil Akin, Roshan Rao, Brian Hie, Zhongkai Zhu, Wenting Lu, Nikita Smetanin, Robert Verkuil, Ori Kabeli, Yaniv Shmueli, et al. Evolutionary-scale prediction of atomic-level protein structure with a language model. *Science*, 379(6637):1123–1130, 2023.
- [20] Minkyung Baek and David Baker. Deep learning and protein structure modeling. *Nature methods*, 19(1):13–14, 2022.
- [21] Ian R Humphreys, Jimin Pei, Minkyung Baek, Aditya Krishnakumar, Ivan Anishchenko, Sergey Ovchinnikov, Jing Zhang, Travis J Ness, Sudeep Banjade, Saket R Bagde, et al. Computed structures of core eukaryotic protein complexes. *Science*, 374(6573):eabm4805, 2021.
- [22] Tomer Tsaban, Julia K Varga, Orly Avraham, Ziv Ben-Aharon, Alisa Khramushin, and Ora Schueler-Furman. Harnessing protein folding neural networks for peptide–protein docking. *Nature communications*, 13(1):1–12, 2022.
- [23] Richard Evans, Michael O’Neill, Alexander Pritzel, Natasha Antropova, Andrew W Senior, Timothy Green, Augustin Židek, Russell Bates, Sam Blackwell, Jason Yim, et al. Protein complex prediction with AlphaFold-Multimer. *BioRxiv*, 2021.

- [24] Patrick Bryant, Gabriele Pozzati, and Arne Elofsson. Improved prediction of protein-protein interactions using alphafold2. *Nature Communications*, 13(1):1–11, 2022.
- [25] Irwin D Kuntz, Jeffrey M Blaney, Stuart J Oatley, Robert Langridge, and Thomas E Ferrin. A geometric approach to macromolecule-ligand interactions. *Journal of molecular biology*, 161(2):269–288, 1982.
- [26] Thomas Lengauer and Matthias Rarey. Computational methods for biomolecular docking. *Current opinion in structural biology*, 6(3):402–406, 1996.
- [27] Jiaying Luo, Wanlei Wei, Jérôme Waldispühl, and Nicolas Moitessier. Challenges and current status of computational methods for docking small molecules to nucleic acids. *European journal of medicinal chemistry*, 168:414–425, 2019.
- [28] Nataraj S Pagadala, Khajamohiddin Syed, and Jack Tuszynski. Software for molecular docking: a review. *Biophysical reviews*, 9:91–102, 2017.
- [29] David Ryan Koes, Matthew P Baumgartner, and Carlos J Camacho. Lessons learned in empirical scoring with smina from the CSAR 2011 benchmarking exercise. *Journal of chemical information and modeling*, 53(8):1893–1904, 2013.
- [30] Sheng-You Huang. Comprehensive assessment of flexible-ligand docking algorithms: current effectiveness and challenges. *Briefings in bioinformatics*, 19(5):982–994, 2018.
- [31] Zhihai Liu, Yan Li, Li Han, Jie Li, Jie Liu, Zhixiong Zhao, Wei Nie, Yuchen Liu, and Renxiao Wang. PDB-wide collection of binding data: current status of the PDBbind database. *Bioinformatics*, 31(3):405–412, 2015.
- [32] Yan Li, Zhihai Liu, Jie Li, Li Han, Jie Liu, Zhixiong Zhao, and Renxiao Wang. Comparative assessment of scoring functions on an updated benchmark: 1. compilation of the test set. *Journal of chemical information and modeling*, 54(6):1700–1716, 2014.
- [33] Gareth Jones, Peter Willett, Robert C Glen, Andrew R Leach, and Robin Taylor. Development and validation of a genetic algorithm for flexible docking. *Journal of molecular biology*, 267(3):727–748, 1997.
- [34] Garrett M Morris, Ruth Huey, William Lindstrom, Michel F Sanner, Richard K Belew, David S Goodsell, and Arthur J Olson. AutoDock4 and AutoDockTools4: Automated docking with selective receptor flexibility. *Journal of computational chemistry*, 30(16):2785–2791, 2009.
- [35] Richard A Friesner, Jay L Banks, Robert B Murphy, Thomas A Halgren, Jasna J Klicic, Daniel T Mainz, Matthew P Repasky, Eric H Knoll, Mee Shelley, Jason K Perry, et al. Glide: a new approach for rapid, accurate docking and scoring. 1. method and assessment of docking accuracy. *Journal of medicinal chemistry*, 47(7):1739–1749, 2004.
- [36] Chao Shen, Xujun Zhang, Yafeng Deng, Junbo Gao, Dong Wang, Lei Xu, Peichen Pan, Tingjun Hou, and Yu Kang. Boosting protein–ligand

- binding pose prediction and virtual screening based on residue–atom distance likelihood potential and graph transformer. *Journal of Medicinal Chemistry*, 65(15):10691–10706, 2022.
- [37] Liangzhen Zheng, Jintao Meng, Kai Jiang, Haidong Lan, Zechen Wang, Mingzhi Lin, Weifeng Li, Hongwei Guo, Yanjie Wei, and Yuguang Mu. Improving protein–ligand docking and screening accuracies by incorporating a scoring function correction term. *Briefings in Bioinformatics*, 23(3):bbac051, 2022.
- [38] Tiziano Tuccinardi, Giulio Poli, Veronica Romboli, Antonio Giordano, and Adriano Martinelli. Extensive consensus docking evaluation for ligand pose prediction and virtual screening studies. *Journal of chemical information and modeling*, 54(10):2980–2986, 2014.
- [39] Chao Shen, Xueping Hu, Junbo Gao, Xujun Zhang, Haiyang Zhong, Zhe Wang, Lei Xu, Yu Kang, Dongsheng Cao, and Tingjun Hou. The impact of cross-docked poses on performance of machine learning classifier for protein–ligand binding pose prediction. *Journal of cheminformatics*, 13(1):1–18, 2021.
- [40] Lorenz M Mayr and Dejan Bojanic. Novel trends in high-throughput screening. *Current opinion in pharmacology*, 9(5):580–588, 2009.
- [41] Seokhyun Moon, Wonho Zhung, Soojung Yang, Jaechang Lim, and Woo Youn Kim. PIGNet: A physics-informed deep learning model toward generalized drug-target interaction predictions. *Chemical Science*, 2022.
- [42] Carmen Gil, Tiziana Ginex, Inés Maestro, Vanesa Nozal, Lucía Barrado-Gil, Miguel Ángel Cuesta-Geijo, Jesús Urquiza, David Ramírez, Covadonga Alonso, Nuria E Campillo, et al. COVID-19: drug targets and potential treatments. *Journal of medicinal chemistry*, 63(21):12359–12386, 2020.
- [43] Shani Zev, Keren Raz, Renana Schwartz, Reem Tarabeh, Prashant Kumar Gupta, and Dan T Major. Benchmarking the ability of common docking programs to correctly reproduce and score binding modes in SARS-CoV-2 protease mpro. *Journal of Chemical Information and Modeling*, 61(6):2957–2966, 2021.
- [44] Dávid Bajusz, Anita Rácz, and Károly Héberger. Why is Tanimoto index an appropriate choice for fingerprint-based similarity calculations? *Journal of cheminformatics*, 7(1):1–13, 2015.
- [45] David Rogers and Mathew Hahn. Extended-connectivity fingerprints. *Journal of chemical information and modeling*, 50(5):742–754, 2010.
- [46] Govinda B Kc, Giovanni Bocci, Srijan Verma, Md Mahmudulla Hassan, Jayme Holmes, Jeremy J Yang, Suman Sirimulla, and Tudor I Oprea. A machine learning platform to estimate anti-SARS-CoV-2 activities. *Nature Machine Intelligence*, 3(6):527–535, 2021.
- [47] Xiangxiang Zeng, Hongxin Xiang, Linhui Yu, Jianmin Wang, Kenli Li, Ruth Nussinov, and Feixiong Cheng. Accurate prediction of molecular properties and drug targets using a self-supervised image representation

- learning framework. *Nature Machine Intelligence*, pages 1–13, 2022.
- [48] Joseph M Paggi, Julia A Belk, Scott A Hollingsworth, Nicolas Vilanueva, Alexander S Powers, Mary J Clark, Augustine G Chemparathy, Jonathan E Tynan, Thomas K Lau, Roger K Sunahara, et al. Leveraging nonstructural data to predict structures and affinities of protein–ligand complexes. *Proceedings of the National Academy of Sciences*, 118(51), 2021.
- [49] Lijuan Yang, Guanghui Yang, Xiaolong Chen, Qiong Yang, Xiaojun Yao, Zhitong Bing, Yuzhen Niu, Liang Huang, and Lei Yang. Deep scoring neural network replacing the scoring function components to improve the performance of structure-based molecular docking. *ACS Chemical Neuroscience*, 12(12):2133–2142, 2021.
- [50] Regine S Bohacek, Colin McMartin, and Wayne C Guida. The art and practice of structure-based drug design: a molecular modeling perspective. *Medicinal research reviews*, 16(1):3–50, 1996.
- [51] Arman A Sadybekov, Anastasiia V Sadybekov, Yongfeng Liu, Christos Iliopoulos-Tsoutsouvas, Xi-Ping Huang, Julie Pickett, Blake Houser, Nilkanth Patel, Ngan K Tran, Fei Tong, et al. Synthon-based ligand discovery in virtual libraries of over 11 billion compounds. *Nature*, pages 1–8, 2021.
- [52] Mengran Fan, Jian Wang, Huaipan Jiang, Yilin Feng, Mehrdad Mahdavi, Kamesh Madduri, Mahmut T Kandemir, and Nikolay V Dokholyan. Gpu-accelerated flexible molecular docking. *The Journal of Physical Chemistry B*, 125(4):1049–1060, 2021.
- [53] Xinqiang Ding, Yujin Wu, Yanming Wang, Jonah Z Vilseck, and Charles L Brooks III. Accelerated CDOCKER with GPUs, parallel simulated annealing, and fast fourier transforms. *Journal of chemical theory and computation*, 16(6):3910–3919, 2020.
- [54] Leonardo Solis-Vasquez, Andreas F Tillack, Diogo Santos-Martins, Andreas Koch, Scott LeGrand, and Stefano Forli. Benchmarking the performance of irregular computations in Autodock-GPU molecular docking. *Parallel Computing*, 109:102861, 2022.
- [55] Francesco Gentile, Vibudh Agrawal, Michael Hsing, Anh-Tien Ton, Fuqiang Ban, Ulf Norinder, Martin E Gleave, and Artem Cherkasov. Deep docking: a deep learning platform for augmentation of structure based drug discovery. *ACS central science*, 6(6):939–949, 2020.
- [56] Stanisław Jastrzębski, Maciej Szymczak, Agnieszka Pocha, Stefan Mordalski, Jacek Tabor, Andrzej J Bojarski, and Sabina Podlewska. Emulating docking results using a deep neural network: a new perspective for virtual screening. *Journal of Chemical Information and Modeling*, 60(9):4246–4262, 2020.
- [57] Biao Ma, Kei Terayama, Shigeyuki Matsumoto, Yuta Isaka, Yoko Sasakura, Hiroaki Iwata, Mitsugu Araki, and Yasushi Okuno. Structure-based de novo molecular generator combined with artificial intelligence and docking simulations. *Journal of Chemical Information and Modeling*,

- 61(7):3304–3313, 2021.
- [58] Yuyang Wang, Jianren Wang, Zhonglin Cao, and Amir Barati Farimani. Molecular contrastive learning of representations via graph neural networks. *Nature Machine Intelligence*, 4(3):279–287, 2022.
- [59] Thai-Hoang Pham, Yue Qiu, Jucheng Zeng, Lei Xie, and Ping Zhang. A deep learning framework for high-throughput mechanism-driven phenotype compound screening and its application to covid-19 drug repurposing. *Nature machine intelligence*, 3(3):247–257, 2021.
- [60] Xiaomin Fang, Lihang Liu, Jieqiong Lei, Donglong He, Shanzhuo Zhang, Jingbo Zhou, Fan Wang, Hua Wu, and Haifeng Wang. Geometry-enhanced molecular representation learning for property prediction. *Nature Machine Intelligence*, 4(2):127–134, 2022.
- [61] Pengyong Li, Jun Wang, Yixuan Qiao, Hao Chen, Yihuan Yu, Xiaojun Yao, Peng Gao, Guotong Xie, and Sen Song. An effective self-supervised framework for learning expressive molecular global representations to drug discovery. *Briefings in Bioinformatics*, 22(6):bbab109, 2021.
- [62] Jeff Guo, Vendy Fialková, Juan Diego Arango, Christian Margreiter, Jon Paul Janet, Kostas Papadopoulos, Ola Engkvist, and Atanas Patronov. Improving de novo molecular design with curriculum learning. *Nature Machine Intelligence*, 4(6):555–563, 2022.
- [63] Michael A Skinnider, R Greg Stacey, David S Wishart, and Leonard J Foster. Chemical language models enable navigation in sparsely populated chemical space. *Nature Machine Intelligence*, 3(9):759–770, 2021.
- [64] Jike Wang, Chang-Yu Hsieh, Mingyang Wang, Xiaorui Wang, Zhenxing Wu, Dejun Jiang, Benben Liao, Xujun Zhang, Bo Yang, Qiaojun He, et al. Multi-constraint molecular generation based on conditional transformer, knowledge distillation and reinforcement learning. *Nature Machine Intelligence*, 3(10):914–922, 2021.
- [65] Sean Ekins, Ana C Puhl, Kimberley M Zorn, Thomas R Lane, Daniel P Russo, Jennifer J Klein, Anthony J Hickey, and Alex M Clark. Exploiting machine learning for end-to-end drug discovery and development. *Nature materials*, 18(5):435–441, 2019.
- [66] Nasim Abdollahi, Ali Madani, Bo Wang, and Stephen MacKinnon. Residue characterization on AlphaFold2 protein structures using graph neural networks. In *NeurIPS*, 2021.
- [67] Pablo Gainza, Freyr Sverrisson, Federico Monti, Emanuele Rodola, D Boscaini, MM Bronstein, and BE Correia. Deciphering interaction fingerprints from protein molecular surfaces using geometric deep learning. *Nature Methods*, 17(2):184–192, 2020.
- [68] Limeng Pu, Rajiv Gandhi Govindaraj, Jeffrey Mitchell Lemoine, Hsiao-Chun Wu, and Michal Brylinski. Deepdrug3d: classification of ligand-binding pockets in proteins with a convolutional neural network. *PLoS computational biology*, 15(2):e1006718, 2019.
- [69] Rishal Aggarwal, Akash Gupta, Vineeth Chelur, CV Jawahar, and

- U Deva Priyakumar. Deep-pocket: ligand binding site detection and segmentation using 3d convolutional neural networks. *Journal of Chemical Information and Modeling*, 2021.
- [70] Bin Huang, Yang Xu, Xiuhong Hu, Yongrui Liu, Shanhui Liao, Jiahai Zhang, Chengdong Huang, Jingjun Hong, Quan Chen, and Haiyan Liu. A backbone-centred energy function of neural networks for protein design. *Nature*, pages 1–6, 2022.
- [71] Ivan Anishchenko, Samuel J Pellock, Tamuka M Chidyausiku, Theresa A Ramelot, Sergey Ovchinnikov, Jingzhou Hao, Khushboo Bafna, Christopher Norn, Alex Kang, Asim K Bera, et al. De novo protein design by deep network hallucination. *Nature*, 600(7889):547–552, 2021.
- [72] Shuang Wang, Tao Song, Shugang Zhang, Mingjian Jiang, Zhiqiang Wei, and Zhen Li. Molecular substructure tree generative model for de novo drug design. *Briefings in Bioinformatics*, 2022.
- [73] Mariya Popova, Olexandr Isayev, and Alexander Tropsha. Deep reinforcement learning for de novo drug design. *Science advances*, 4(7):eaap7885, 2018.
- [74] Mingyang Wang, Huiyong Sun, Jike Wang, Jinping Pang, Xin Chai, Lei Xu, Honglin Li, Dongsheng Cao, and Tingjun Hou. Comprehensive assessment of deep generative architectures for de novo drug design. *Briefings in Bioinformatics*, 23(1):bbab544, 2022.
- [75] W Patrick Walters and Regina Barzilay. Applications of deep learning in molecule generation and molecular property prediction. *Accounts of chemical research*, 54(2):263–270, 2020.
- [76] Qifeng Bai, Shuoyan Tan, Tingyang Xu, Huanxiang Liu, Junzhou Huang, and Xiaojun Yao. MolAICal: a soft tool for 3D drug design of protein targets by artificial intelligence and classical algorithm. *Briefings in bioinformatics*, 22(3):bbaa161, 2021.
- [77] Xiaoqi Wang, Bin Xin, Weihong Tan, Zhijian Xu, Kenli Li, Fei Li, Wu Zhong, and Shaoliang Peng. DeepR2cov: deep representation learning on heterogeneous drug networks to discover anti-inflammatory agents for COVID-19. *Briefings in bioinformatics*, 22(6):bbab226, 2021.
- [78] Sowmya Ramaswamy Krishnan, Navneet Bung, Gopalakrishnan Bulusu, and Arijit Roy. Accelerating de novo drug design against novel proteins using deep learning. *Journal of Chemical Information and Modeling*, 61(2):621–630, 2021.
- [79] Michael Moret, Moritz Helmstädter, Francesca Grisoni, Gisbert Schneider, and Daniel Merk. Beam search for automated design and scoring of novel ROR ligands with machine intelligence. *Angewandte Chemie International Edition*, 60(35):19477–19482, 2021.
- [80] Helen Berman, Kim Henrick, and Haruki Nakamura. Announcing the worldwide protein data bank. *Nature Structural & Molecular Biology*, 10(12):980–980, 2003.
- [81] Greg Landrum et al. Rdkit: Open-source cheminformatics. 2006.
- [82] David S Wishart, Yannick D Feunang, An C Guo, Elvis J Lo, Ana Marcu,

- Jason R Grant, Tanvir Sajed, Daniel Johnson, Carin Li, Zinat Sayeeda, et al. Drugbank 5.0: a major update to the drugbank database for 2018. *Nucleic acids research*, 46(D1):D1074–D1082, 2018.
- [83] Anna Gaulton, Louisa J Bellis, A Patricia Bento, Jon Chambers, Mark Davies, Anne Hersey, Yvonne Light, Shaun McGlinchey, David Michalovich, Bissan Al-Lazikani, et al. ChEMBL: a large-scale bioactivity database for drug discovery. *Nucleic acids research*, 40(D1):D1100–D1107, 2012.
- [84] Jun Xia, Yanqiao Zhu, Yuanqi Du, and Stan Z Li. Pre-training graph neural networks for molecular representations: Retrospect and prospect. In *ICML 2022 2nd AI for Science Workshop*.
- [85] Helen M Berman, John Westbrook, Zukang Feng, Gary Gilliland, Talapady N Bhat, Helge Weissig, Ilya N Shindyalov, and Philip E Bourne. The protein data bank. *Nucleic acids research*, 28(1):235–242, 2000.
- [86] Minyi Su, Qifan Yang, Yu Du, Guoqin Feng, Zhihai Liu, Yan Li, and Renxiao Wang. Comparative assessment of scoring functions: the CASF-2016 update. *Journal of chemical information and modeling*, 59(2):895–913, 2018.
- [87] Brian J Bender, Stefan Gahbauer, Andreas Luttmens, Jiankun Lyu, Chase M Webb, Reed M Stein, Elissa A Fink, Trent E Balius, Jens Carlsson, John J Irwin, et al. A practical guide to large-scale docking. *Nature protocols*, 16(10):4799–4832, 2021.
- [88] Thomas A Halgren. Identifying and characterizing binding sites and assessing druggability. *Journal of chemical information and modeling*, 49(2):377–389, 2009.
- [89] Alasdair TR Laurie and Richard M Jackson. Q-SiteFinder: an energy-based method for the prediction of protein–ligand binding sites. *Bioinformatics*, 21(9):1908–1916, 2005.
- [90] Narayanan Eswar, David Eramian, Ben Webb, Min-Yi Shen, and Andrej Sali. Protein structure modeling with modeller. In *Structural proteomics*, pages 145–159. Springer, 2008.
- [91] Vincent Le Guilloux, Peter Schmidtke, and Pierre Tuffery. Fpocket: an open source platform for ligand pocket detection. *BMC bioinformatics*, 10(1):1–11, 2009.
- [92] Dominik Gront, Sebastian Kmiecik, and Andrzej Kolinski. Backbone building from quadrilaterals: a fast and accurate algorithm for protein backbone reconstruction from alpha carbon coordinates. *Journal of computational chemistry*, 28(9):1593–1597, 2007.
- [93] Sebastian Kmiecik, Dominik Gront, Michal Kolinski, Lukasz Wieteska, Aleksandra Elzbieta Dawid, and Andrzej Kolinski. Coarse-grained protein models and their applications. *Chemical reviews*, 116(14):7898–7936, 2016.
- [94] Petar Velickovic, Guillem Cucurull, Arantxa Casanova, Adriana Romero, Pietro Lio, and Yoshua Bengio. Graph attention networks. *stat*, 1050:20, 2017.

- [95] Victor Garcia Satorras, Emiel Hooeboom, and Max Welling. E (n) equivariant graph neural networks. *arXiv preprint arXiv:2102.09844*, 2021.
- [96] Noel M O’Boyle, Michael Banck, Craig A James, Chris Morley, Tim Vandermeersch, and Geoffrey R Hutchison. Open Babel: An open chemical toolbox. *Journal of cheminformatics*, 3(1):1–14, 2011.
- [97] Vijay Prakash Dwivedi and Xavier Bresson. A generalization of transformer networks to graphs. *arXiv preprint arXiv:2012.09699*, 2020.
- [98] Yunsheng Shi, Zhengjie Huang, Shikun Feng, Hui Zhong, Wenjin Wang, and Yu Sun. Masked label prediction: Unified message passing model for semi-supervised classification. *arXiv preprint arXiv:2009.03509*, 2020.
- [99] Jimmy Lei Ba, Jamie Ryan Kiros, and Geoffrey E Hinton. Layer normalization. *arXiv preprint arXiv:1607.06450*, 2016.
- [100] Weihua Hu, Bowen Liu, Joseph Gomes, Marinka Zitnik, Percy Liang, Vijay Pande, and Jure Leskovec. Strategies for pre-training graph neural networks. *arXiv preprint arXiv:1905.12265*, 2019.
- [101] Tsung-Yi Lin, Priya Goyal, Ross Girshick, Kaiming He, and Piotr Dollár. Focal loss for dense object detection. In *Proceedings of the IEEE international conference on computer vision*, pages 2980–2988, 2017.
- [102] Thomas A Halgren. Merck molecular force field. i. basis, form, scope, parameterization, and performance of mmff94. *Journal of computational chemistry*, 17(5-6):490–519, 1996.
- [103] Thomas Gaillard. Evaluation of Autodock and Autodock Vina on the CASF-2013 benchmark. *Journal of chemical information and modeling*, 58(8):1697–1706, 2018.
- [104] Na Zhang and Hongtao Zhao. Enriching screening libraries with bioactive fragment space. *Bioorganic & Medicinal Chemistry Letters*, 26(15):3594–3597, 2016.
- [105] Sebastian Salentin, Sven Schreiber, V Joachim Haupt, Melissa F Adasme, and Michael Schroeder. PLIP: fully automated protein–ligand interaction profiler. *Nucleic acids research*, 43(W1):W443–W447, 2015.
- [106] Marta M Stepniewska-Dziubinska, Piotr Zielenkiewicz, and Pawel Siedlecki. Development and evaluation of a deep learning model for protein–ligand binding affinity prediction. *Bioinformatics*, 34(21):3666–3674, 2018.
- [107] Zixuan Cang and Guo-Wei Wei. TopologyNet: Topology based deep convolutional and multi-task neural networks for biomolecular property predictions. *PLoS computational biology*, 13(7):e1005690, 2017.
- [108] Derek Jones, Hyojin Kim, Xiaohua Zhang, Adam Zemla, Garrett Stevenson, WF Drew Bennett, Daniel Kirshner, Sergio E Wong, Felice C Lightstone, and Jonathan E Allen. Improved protein–ligand binding affinity prediction with structure-based deep fusion inference. *Journal of chemical information and modeling*, 61(4):1583–1592, 2021.
- [109] Liangzhen Zheng, Jingrong Fan, and Yuguang Mu. Onionnet: a multiple-layer intermolecular-contact-based convolutional neural network for

- protein–ligand binding affinity prediction. *ACS omega*, 4(14):15956–15965, 2019.
- [110] Dejun Jiang, Chang-Yu Hsieh, Zhenxing Wu, Yu Kang, Jike Wang, Ercheng Wang, Ben Liao, Chao Shen, Lei Xu, Jian Wu, et al. InteractionGraphNet: A novel and efficient deep graph representation learning framework for accurate protein–ligand interaction predictions. *Journal of medicinal chemistry*, 64(24):18209–18232, 2021.
- [111] Yeji Wang, Shuo Wu, Yanwen Duan, and Yong Huang. A point cloud-based deep learning strategy for protein–ligand binding affinity prediction. *Briefings in Bioinformatics*, 23(1):bbab474, 2022.
- [112] Huimin Shen, Youzhi Zhang, Chunhou Zheng, Bing Wang, and Peng Chen. A cascade graph convolutional network for predicting protein–ligand binding affinity. *International journal of molecular sciences*, 22(8):4023, 2021.
- [113] Gabriele Corso, Hannes Stärk, Bowen Jing, Regina Barzilay, and Tommi Jaakkola. Diffdock: Diffusion steps, twists, and turns for molecular docking. *arXiv preprint arXiv:2210.01776*, 2022.
- [114] Saul B Needleman and Christian D Wunsch. A general method applicable to the search for similarities in the amino acid sequence of two proteins. *Journal of molecular biology*, 48(3):443–453, 1970.
- [115] Lagnajit Pattanaik and Connor W Coley. Molecular representation: going long on fingerprints. *Chem*, 6(6):1204–1207, 2020.